The Astrophysical Journal, 783:131 (27pp), 2014 March 10 doi:10.1088/0004-637X/783/2/131

PROPERTIES OF THE REMNANT CLOCKWISE DISK OF YOUNG STARS IN THE GALACTIC CENTER

S. Yelda[1], A. M. Ghez[1], J. R. Lu[2], T. Do[3], L. Meyer[1], M. R. Morris[1], and K. Matthews[4]
[1] UCLA Department of Physics and Astronomy, Los Angeles, CA 90095-1547, USA; syelda@astro.ucla.edu, ghez@astro.ucla.edu, leo@astro.ucla.edu, morris@astro.ucla.edu
[2] Institute for Astronomy, University of Hawaii, Honolulu, HI 96822, USA; jlu@ifa.hawaii.edu
[3] Dunlap Institute for Astronomy and Astrophysics, University of Toronto, 50 St. George Street, Toronto M5S 3H4, ON, Canada; do@di.utoronto.ca
[4] Astrophysics, California Institute of Technology, MC 249-17, Pasadena, CA 91125, USA; kym@caltech.edu
Received 2013 June 17; accepted 2014 January 30; published 2014 February 24

ABSTRACT

We present new kinematic measurements and modeling of a sample of 116 young stars in the central parsec of the Galaxy in order to investigate the properties of the young stellar disk. The measurements were derived from a combination of speckle and laser guide star adaptive optics imaging and integral field spectroscopy from the Keck telescopes. Compared to earlier disk studies, the most important kinematic measurement improvement is in the precision of the accelerations in the plane of the sky, which have a factor of six smaller uncertainties ($\sigma \sim 10$ μas yr^{-2}). We have also added the first radial velocity measurements for eight young stars, increasing the sample at the largest radii (6″–12″) by 25%. We derive the ensemble properties of the observed stars using Monte Carlo simulations of mock data. There is one highly significant kinematic feature ($\sim 20\sigma$), corresponding to the well-known clockwise disk, and no significant feature is detected at the location of the previously claimed counterclockwise disk. The true disk fraction is estimated to be $\sim$20%, a factor of $\sim$2.5 lower than previous claims, suggesting that we may be observing the remnant of what used to be a more densely populated stellar disk. The similarity in the kinematic properties of the B stars and the O/WR stars suggests a common star formation event. The intrinsic eccentricity distribution of the disk stars is unimodal, with an average value of $\langle e \rangle = 0.27 \pm 0.07$, which we show can be achieved through dynamical relaxation in an initially circular disk with a moderately top-heavy mass function.

Key words: astrometry – Galaxy: center – infrared: stars – techniques: high angular resolution

Online-only material: color figures, machine-readable table

1. INTRODUCTION

Spectroscopic observations of the Galaxy's central parsec have revealed an enigmatic population of nearly 200 hot, early-type stars, including Wolf–Rayet (WR) stars and O and B type main sequence stars, giants, and supergiants (Allen et al. 1990; Krabbe et al. 1991, 1995; Blum et al. 1995; Tamblyn et al. 1996; Najarro et al. 1997; Ghez et al. 2003; Paumard et al. 2006; Bartko et al. 2010; Do et al. 2013). Their location in the Galactic center (GC) raises the question of how stars can form in such a hostile environment, as the tidal forces from the 4×10^6 $M_\odot$ supermassive black hole (SMBH; Ghez et al. 2008; Gillessen et al. 2009) would prevent the collapse of typical molecular clouds within its radius of influence ($r_{\rm infl} \sim 2$ pc; Sanders 1992; Morris 1993).

Clues to the origin of these stars can be gained through the detailed study of their orbital dynamics, as the age of the population ($\sim$3–8 Myr; Paumard et al. 2006; Lu et al. 2013) is much less than the relaxation timescale in the GC ($\sim$1 Gyr; Hopman & Alexander 2006). A particularly prominent feature that has been observed is a stellar disk containing a large fraction of the O and WR stars orbiting the black hole in a clockwise (CW) sense, with an inner edge at a projected radius of $R = 0.''8$ (Levin & Beloborodov 2003; Genzel et al. 2003; Paumard et al. 2006; Lu et al. 2009; Bartko et al. 2009). At smaller radii, dynamical effects such as vector resonant relaxation (Rauch & Tremaine 1996; Hopman & Alexander 2006; Alexander 2007) will randomize the orbital planes within the lifetimes of the B stars, which is in agreement with observations (Schödel et al. 2003; Ghez et al. 2005b; Eisenhauer et al. 2005; Gillessen et al. 2009). The coherent motion of the disk stars may be indicative of in situ formation in a massive, gas disk around the SMBH (Levin & Beloborodov 2003). In standard models of accretion disks around central black holes, the disks are expected to fragment under their own self-gravity and lead to the formation of stars (Kolykhalov & Syunyaev 1980; Shlosman & Begelman 1987; Goodman 2003; Nayakshin 2006; Nayakshin et al. 2007). In such models, the steady build-up of the gas disk leads to stars on circular orbits, as the gas will have circularized prior to star formation. However, there is growing evidence that the young stars are on more eccentric orbits (Paumard et al. 2006; Beloborodov et al. 2006; Lu et al. 2009; Bartko et al. 2009; Gillessen et al. 2009). Several theories have invoked the infall of giant molecular clouds or the collision of two clouds to produce initially eccentric stellar disks (Mapelli et al. 2008; Yusef-Zadeh & Wardle 2008; Wardle & Yusef-Zadeh 2008; Bonnell & Rice 2008). In any case, the surface density predicted by in situ formation scenarios falls off like r^{-2} (Lin & Pringle 1987; Levin 2007) and agrees well with observations of the disk (Paumard et al. 2006; Lu et al. 2009; Bartko et al. 2009).

A stellar disk may also result from the inward migration of a massive cluster whose stars are tidally stripped as it spirals inward under dynamical friction (Gerhard 2001). However, this theory has been difficult to reconcile with observations, most notably the surface density profile. During the infall, the cluster will deposit stars throughout the GC with a radial profile of $r^{-0.75}$, much shallower than that observed (Berukoff & Hansen 2006). Furthermore, in order for the cluster to reach the small galactocentric radii that the young stars occupy, unrealistic cluster properties are required, such as an initial cluster mass of $>10^5$ $M_\odot$ or the presence of an intermediate mass black hole (IMBH; Hansen & Milosavljević 2003; Gürkan & Rasio 2005;

Berukoff & Hansen 2006) containing too large a fraction of the total cluster mass (Kim et al. 2004).

While there is consensus in the literature regarding the existence of the CW disk and its surface density profile, many of its properties have yet to be well characterized, in part because interpretations of kinematic studies rely on the ability to assign disk membership. For example, Bartko et al. (2009) reported a bimodal eccentricity distribution for the disk, which is difficult to explain dynamically. The authors could not rule out that contamination by non-members of the disk led to the second peak seen at $e = 0.9$–1.0. Contamination may also affect the interpretation of the geometric structure of the disk, which was recently claimed to be highly warped (Bartko et al. 2009).

Further controversy exists regarding the kinematic properties of the stars that are not on the CW disk. Claims of a second, counterclockwise disk have been made (Genzel et al. 2003; Paumard et al. 2006), although this structure was not detected by Lu et al. (2009) and was later reinterpreted as a possible streamer or dissolving disk by Bartko et al. (2009). Precise orbital parameter estimates are necessary for resolving this issue, as the presence of a second structure has implications for both star formation and stellar dynamical evolution in the GC.

We have carried out a detailed kinematic analysis on the GC's young star population using high precision astrometric measurements over a 16 yr baseline. Both the size and radial extent of our sample have increased by a factor of ∼3–4 over our previous efforts in Lu et al. (2009). The data sets and sample are presented in Section 2. The data analysis, including image processing and astrometric and orbital analysis techniques, is detailed in Section 3. To explore the impacts of measurement error and the assumptions used in our analysis, simulations are run on mock data sets, which are presented in parallel with the observed results in Section 4. We discuss our findings in Section 5 and conclude in Section 6.

2. SAMPLE AND DATA SETS

2.1. Sample

There are 116 stars that form the sample of this study (see Figure 1). These stars are selected based on the following two criteria.

1. *Spectroscopic selection criteria:* stars that are spectroscopically identified as young and have spectral line measurements with sufficient signal-to-noise ratio (S/N) to measure a radial velocity (RV). We use both existing RV measurements (Paumard et al. 2006; Bartko et al. 2009) and new measurements based on spectroscopic data reported in Do et al. (2009, 2013).
2. *Location selection criteria:* located outside a projected radius of $R = 0\farcs8$, which has been previously identified as the inner edge of the CW disk (Paumard et al. 2006) since stars interior to this radius appear to be randomly oriented (Schödel et al. 2003; Ghez et al. 2005b; Gillessen et al. 2009), and within a $27'' \times 27''$ region that is centered roughly on Sgr A* and that is defined by our widest imaging field of view (FOV; see next section).

We assume initially that all of the young stars meeting the above criteria belong to the same population since the estimated age of the O/WR stars is ∼3–8 Myr (Paumard et al. 2006; Lu et al. 2013) and the B stars have main sequence lifetimes of up to ∼30 Myr for the faintest stars in our sample ($K = 15.9$). We explicitly test this assumption in Section 5.4 by separating the sample into two subsets based on K magnitude.

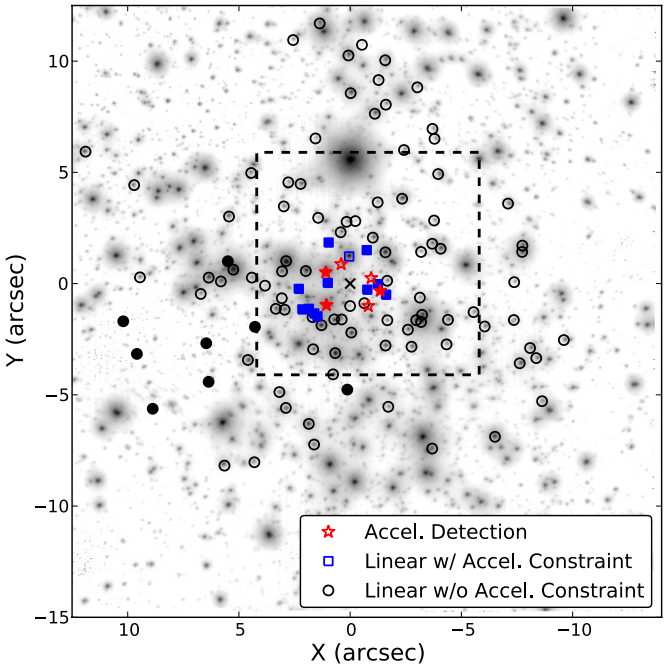

Figure 1. Location of the 116 young stars with RV and astrometric measurements that comprise the sample for this study. Sources are identified based on their astrometric properties: acceleration detections (red stars), linearly moving with acceleration constraints (blue squares), and linearly moving without acceleration constraints (black circles). Filled stars and filled squares mark sources with new acceleration detections and acceleration constraints, while the filled circles mark the sources with new radial velocity measurements from GCOWS. In the background is the wide-field adaptive optics mosaic image from 2008 May covering the central ∼1 pc of the Galaxy. The dashed black box denotes the central $10''$ field of view where the highest astrometric precision is achieved.

(A color version of this figure is available in the online journal.)

2.2. Imaging Observations

The astrometric measurements in this study are based on three types of high-angular resolution 2 μm imaging observations (speckle imaging, narrow-field adaptive optics imaging, wide-field mosaic AO imaging), which have been obtained at the W. M. Keck observatory over a 16 yr time period. As has been reported in previous publications (Ghez et al. 1998, 2000, 2005b, 2008; Lu et al. 2009), the earliest data sets were obtained with K-band (2.2 μm) speckle imaging between 1995 and 2005 using the Near Infrared Camera (NIRC; Matthews & Soifer 1994; Matthews et al. 1996), which has a $\sim 5'' \times 5''$ FOV. From the 27 epochs of available speckle data, we use those epochs with more than 900 frames to insure robust coordinate transformations (see Section 3.1.3). This excludes only 2000 April (805 frames), resulting in 26 speckle epochs with a time baseline of 10 yr (see Table 1).

Since 2004, we have utilized the Keck II adaptive optics (AO) system in conjunction with the facility near infrared camera NIRC2 (PI: K. Matthews) in its narrow-field mode, which has a plate scale of 9.952 mas pix^{-1} (Yelda et al. 2010) and a $10''$ FOV (∼0.4 pc at the 8 kpc distance to the GC; Ghez et al. 2008). Here we include all existing Keck AO observations through 2011, which includes 19 epochs and a time baseline of seven years (Ghez et al. 2005a, 2008; Lu et al. 2009; Meyer et al. 2012). As compared to our previous work on the young stars in Lu et al. (2009), which included only two years of deep,

Table 1
Summary of Speckle Imaging Observations

Date (UT)	Frames Obtained	Frames Used	FWHM (mas)	Strehl	N_{stars}	K_{lim}[a] (mag)	σ_{pos}[b] (mas)	Data Source[c]
1995 Jun 9–12	15114	1800	57	0.06	151	15.4	1.06	Ref. 1
1996 Jun 26–27	9261	865	60	0.03	77	14.1	1.76	Ref. 1
1997 May 14	3811	1837	61	0.04	139	15.4	1.28	Ref. 1
1998 Apr 2–3	9751	1639	62	0.04	83	14.6	1.52	Ref. 2
1998 May 14–15	16531	2102	69	0.04	126	15.4	1.32	Ref. 2
1998 Jul 3–5	9751	933	61	0.06	127	15.3	1.24	Ref. 2
1998 Aug 4–6	20375	1933	61	0.06	172	15.6	0.84	Ref. 2
1998 Oct 9	4776	1082	55	0.07	120	15.3	1.49	Ref. 2
1999 May 2–4	19512	1857	70	0.07	183	15.7	1.06	Ref. 2
1999 Jul 24–25	19307	2108	55	0.09	232	15.8	0.75	Ref. 2
2000 May 19–20	21492	2492	55	0.08	242	15.8	0.67	Ref. 3
2000 Jul 19–20	15124	1581	61	0.07	194	15.6	1.11	Ref. 3
2000 Oct 18	2587	1517	59	0.04	77	14.4	1.34	Ref. 3
2001 May 7–9	11343	1994	54	0.07	175	15.5	1.03	Ref. 3
2001 Jul 28–29	15920	1695	54	0.11	239	16.0	0.79	Ref. 3
2002 Apr 23–24	16130	1958	66	0.05	183	15.7	1.15	Ref. 3
2002 May 23–24	18338	1443	58	0.08	252	15.8	0.85	Ref. 3
2002 Jul 19–20	8878	1118	61	0.06	125	15.3	1.40	Ref. 3
2003 Apr 21–22	14475	1841	61	0.04	121	15.3	1.06	Ref. 3
2003 Jul 22–23	6948	1703	64	0.07	180	15.7	1.17	Ref. 3
2003 Sep 7–8	9799	1723	63	0.07	182	15.7	1.22	Ref. 3
2004 Apr 29–30	20140	1423	62	0.08	185	15.7	0.75	Ref. 4
2004 Jul 25–26	14440	2161	59	0.08	200	15.7	0.86	Ref. 4
2004 Aug 29	3040	1301	57	0.08	167	15.6	1.25	Ref. 4
2005 Apr 24–25	15770	1679	59	0.06	162	15.6	0.99	Ref. 5
2005 Jul 26–27	14820	1331	60	0.05	111	15.2	1.19	Ref. 5

Notes.
[a] K_{lim} is the magnitude at which the cumulative distribution function of the observed K magnitudes reaches 90% of the total sample size.
[b] Positional error taken as error on the mean from the three sub-images in each epoch and includes stars with $K < 15$.
[c] Data originally reported in (1) Ghez et al. (1998), (2) Ghez et al. (2000), (3) Ghez et al. (2005b), (4) Lu et al. (2005), and (5) Rafelski et al. (2007).

narrow-field AO imaging observations, we tripled the time baseline for this type of observation. The observational setup was the same as the 2006–2007 laser guide star adaptive optics (LGSAO) observations reported in Ghez et al. (2008). Specifically, a 20-point pseudo-random $0\farcs7 \times 0\farcs7$ dither pattern was used, with an initial position that placed IRS 16NE at pixel (229, 720). The images were taken at a position angle (P.A.) of 0°, and each frame consisted of 10 co-added 2.8 s integrations. At least three exposures were taken at each dither position. The star USNO 0600-28577051 ($R = 13.7$ mag and $\Delta r_{Sgr\,A^*} = 19''$) was used to correct for tip and tilt in the LGSAO observations and served as the natural guide star in the NGSAO observation of the GC. Table 2 summarizes the narrow-field AO imaging observations used in this study.

To measure the proper motions of the young stars at larger radii from Sgr A* ($R \gtrsim 7''$), we obtained three epochs of K'-band LGSAO mosaics with the NIRC2 narrow camera that cover $27'' \times 27''$ (~1.1 pc × 1.1 pc). These observations were taken on 2006 May 3, 2008 May 20, and 2010 June 5. The tip-tilt star, P.A., filter, exposure time per frame, and initial position were the same as those used for the deep narrow-field AO imaging data set, which covered the central $10'' \times 10''$. In order to obtain the large FOV, we used a nine-position box pattern with a $8\farcs5$ dither offset and obtained 3–7 frames at each dither position. For the first two epochs, we also obtained a four-position box pattern with $4''$ dithers, providing large overlaps between all tiles in the mosaic. At least three exposures were taken at each dither position. We refer to these wide-field data as "mosaics" and the details of the observations can be found in Table 3.

2.3. Spectroscopic Observations

To spectroscopically identify young stars and measure their line-of-sight motions, high angular resolution spectroscopic observations were obtained with the integral field spectrograph OSIRIS in conjunction with the LGSAO system on Keck II (Larkin et al. 2006). The central $4''$ have been observed since 2006 with the Kn3 narrowband filter centered on the Brγ line ($\lambda = 2.1661$ μm) and using the 35 mas plate scale. In 2010, we began the Galactic Center OSIRIS Wide-field Survey (GCOWS), in which observations were taken along the eastern portion of the CW disk in order to maximize the number of young star identifications (Do et al. 2013). These observations reached a radial extent of $R \sim 14''$ east of Sgr A* and used the 50 mas plate scale. The details of our OSIRIS observations are presented in Ghez et al. (2008) and Do et al. (2009, 2013). While the spectroscopic identification of young stars using OSIRIS has been reported elsewhere (Do et al. 2009, 2013), we report the RVs for 38 stars from this instrument for the first time here. For eight of these stars, this is the first report of an RV measurement in the literature.

3. DATA ANALYSIS

3.1. Astrometry

3.1.1. Image Processing

All data sets were reduced using standard data processing techniques, including sky subtraction, flat-fielding, and bad-pixel and cosmic-ray rejection. The AO data were corrected

Table 2
Summary of AO Imaging Observations

Date (UT)	Frames Obtained	Frames Used	FWHM (mas)	Strehl	N_{stars}	K_{lim}[a] (mag)	σ_{pos}[b] (mas)	Data Source[c]
2004 Jul 26	10	10	60	0.28	598	15.9	0.30	LGSAO; Ref. 6
2005 Jun 30	10	10	61	0.26	929	16.3	0.32	LGSAO; Ref. 8
2005 Jul 31	59	31	57	0.18	1865	19.0	0.10	LGSAO; Ref. 7
2006 May 2–3	153	107	58	0.24	1952	19.1	0.05	LGSAO; Ref. 7
2006 Jun 19–20	289	156	57	0.30	2460	19.5	0.08	LGSAO; Ref. 7
2006 Jul 16	70	64	58	0.28	2179	19.3	0.09	LGSAO; Ref. 7
2007 May 17	101	76	58	0.28	2514	19.4	0.09	LGSAO; Ref. 7
2007 Aug 11–12	139	78	57	0.24	1879	19.0	0.08	LGSAO; Ref. 7
2008 May 15	138	134	54	0.25	2089	19.4	0.06	LGSAO; Ref. 9
2008 Jul 24	179	104	58	0.27	2189	19.3	0.04	LGSAO; Ref. 9
2009 May 4	311	149	57	0.27	2316	19.2	0.08	LGSAO; Ref. 9
2009 Jul 24	146	75	62	0.21	1701	18.9	0.09	LGSAO; Ref. 9
2009 Sep 9	55	43	61	0.25	1921	18.9	0.11	LGSAO; Ref. 9
2010 May 5	219	158	63	0.23	2037	19.1	0.06	LGSAO; Ref. 9
2010 Jul 6	136	117	61	0.23	1956	18.9	0.08	LGSAO; Ref. 9
2010 Aug 15	143	127	60	0.21	1826	19.0	0.07	LGSAO; Ref. 9
2011 May 27	164	114	66	0.19	1563	18.8	0.13	LGSAO; Ref. 9
2011 Jul 18	212	167	59	0.21	2031	19.2	0.08	NGSAO; Ref. 9
2011 Aug 23	218	196	59	0.27	2372	19.4	0.05	LGSAO; Ref. 9

Notes.
[a] K_{lim} is the magnitude at which the cumulative distribution function of the observed K magnitudes reaches 90% of the total sample size.
[b] Positional error taken as error on the mean from the three sub-images in each epoch and includes stars with $K < 15$.
[c] Data originally reported in (6) Ghez et al. (2005a), (7) Ghez et al. (2008), (8) Lu et al. (2009), and (9) Yelda (2012) and this work.

Table 3
Summary of Wide-field Mosaic Observations

Date (UT)	N Dither Positions	$\langle N_{frmObtained} \rangle$ per Position	$\langle N_{frmUsed} \rangle >$ per Position	FWHM (mas)	Strehl	N_{stars}	K_{lim}[a] (mag)	σ_{pos}[b] (mas)	Data Source[c]
2006 May 3	13	3.4	3.4	63	0.20	6583	18.1	1.63	LGSAO; Ref. 10
2008 May 20	13	3.4	2.9	78	0.11	4494	17.1	1.88	LGSAO; Ref. 10
2010 Jun 5	9	7.2	5.4	76	0.12	5189	17.6	1.71	LGSAO; Ref. 10

Notes.
[a] K_{lim} is the magnitude at which the cumulative distribution function of the observed K magnitudes reaches 90% of the total sample size.
[b] Positional errors include distortion error (see text).
[c] Data originally reported in (10) Do et al. (2013).

for both optical distortion using the latest solution for the NIRC2 narrow camera and achromatic differential atmospheric refraction (Yelda et al. 2010). Based on this distortion solution, we derive an improved solution for the NIRC speckle camera (Appendix A) using an approach similar to that of Lu et al. (2009). The updated NIRC distortion coefficients are presented in Table 7.

For each observing run, individual frames are combined to make an average map. The details of this process depend on the observing technique used. The speckle data are combined to create an average image for each epoch using a weighted shift-and-add technique as described in Hornstein (2007). The final speckle images cover an FOV of $\sim 6'' \times 6''$, centered approximately on Sgr A*. For the AO narrow-field data, frames are selected based on the image quality, as measured by the full width at half-maximum (FWHM) of the point-spread function (PSF). We choose to keep only those frames whose FWHM is within 125% of the minimum observed FWHM measured in a given epoch. These images are then combined with a weighted average, where the weights are set equal to the Strehl ratio of each image. For each epoch of mosaic data, we create an average image at each dither position (i.e., 13 for each of the 2006 and 2008 observations, and 9 for the 2010 observation). All exposures taken at a given dither position are included in the corresponding average image except for a few cases where the frames were of extremely poor quality for one of several reasons (e.g., clouds or laser collision with neighboring telescopes). As done in our previous efforts, we create three independent subset images of equivalent quality in order to determine astrometric and photometric uncertainties for the speckle and AO central $10''$ images. Likewise, subset images are created for each of the individual dither positions in the mosaics.

3.1.2. Star Lists

Stars are identified and their relative positions and brightnesses are extracted from all images using the PSF fitting algorithm *StarFinder* (Diolaiti et al. 2000), which is optimized for AO observations of crowded stellar fields to identify and characterize stars in the FOV. A model PSF for each image is iteratively constructed based on a set of bright stars in the field that have been pre-selected by the user. The model PSF is then cross-correlated with the image in order to identify sources in the field. The stars that are input for PSF construction are IRS 16C, 16NW, and 16NE for the speckle images, and IRS 16C, 16NW, 16SW, 16NE, 29, 33E, S1-23, S2-16, and S3-22 for the

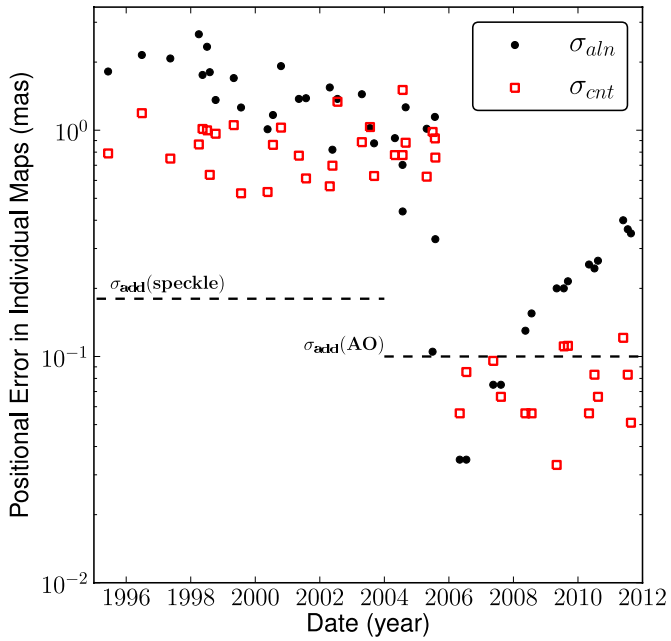

Figure 2. Relative astrometric uncertainties, including alignment (filled black points) and centroiding (unfilled red squares) uncertainties as a function of epoch for speckle data from 1995 to 2005 and central 10″ AO data from 2004 to 2011. The median uncertainty of the young stars is reported for each epoch. Alignment errors are minimized near the reference epoch, 2006 June, and increase with time away from this epoch (see Section 3.1.3). All epochs with $\sigma_{\rm aln} > 0.5$ mas are from speckle imaging, where the higher uncertainties are a result of very few reference stars as compared to AO data. The additive errors for speckle and AO are shown as dashed lines.

(A color version of this figure is available in the online journal.)

central 10″ AO images. The set of PSF stars used for each image in the mosaic, on the other hand, depends on the position of that image within the wide mosaic FOV. These stars include the aforementioned sources for the central 10″ AO data set, as well as the following stars: IRS 1NE, 1SE, 2, 7, 9, 10EE, 10E3, 12N, 14SW, 14NE, 28, 34W, S5-183, S5-69, S8-3, S8-8, S9-3, S9-9, S10-2, S10-3, S11-4, S11-6, S9-5, S12-2, S13-61. To identify sources, we use a *StarFinder* correlation threshold of 0.8 in the average image and 0.6 in each of the three subset images. The initial star list for each epoch contains only those sources that are detected in the average image and in all three subset images. The inaccuracies in the PSF model for the AO images occasionally lead to spurious source detections near bright stars. We therefore use the procedure described in Appendix A of Yelda et al. (2010) to remove these false sources (∼20% of the sources identified). Altogether, we identify 162 and 1915 stars on average in the speckle ($\langle K_{\rm lim}\rangle = 15.4$) and AO data sets ($\langle K_{\rm lim}\rangle = 18.8$), respectively.

There are two sources of statistical uncertainty associated with each positional measurement in the narrow-field images. First is the centroiding uncertainty ($\sigma_{\rm cnt}$), which is taken as the error on the mean of the positions for each star in the three subset images. Second, there is a term that appears to arise from inaccuracies in the estimates of the PSF wings of neighboring sources (Fritz et al. 2010). As described in Appendix B, we follow a procedure similar to Clarkson et al. (2012), and estimate this additive error term ($\sigma_{\rm add}$) to be 0.18 mas and 0.10 mas for the speckle and central 10″ observations, respectively. Figure 2 shows the centroiding and additive errors for each of our speckle and central 10″ data sets. In addition, three of the AO data sets were taken at either different positions or position angles than the rest of the AO observations and therefore are impacted by residual distortion left over after the distortion correction is applied, as described in Yelda et al. (2010). We account for the effects of residual distortion in these images by performing a local distortion correction (Appendix C), which adds 0.5–1.4 mas errors to these epochs. The centroiding uncertainties in the speckle data are typically a factor of ∼5 larger than the additive error and therefore dominate the error budget. For the AO data, these two error terms are comparable ($\sigma_{\rm cnt} \sim 0.1$ mas).

The speckle observations were taken in stationary mode, and so the field rotated over the course of the night. This led to an FOV with varying numbers of frames contributing to each pixel in the final image. As a result, stars near the edges of the FOV had relatively poor astrometric measurements. To account for this effect, we require that each source be at a location in the average map that was covered by at least 80% of the frames contributing to that map.[5] This prevented edge effect problems for these data sets, which had much less uniform coverage than the AO data sets. In total, 459 combined detections from 45 stars were removed, which is equivalent to 47% of all young star measurements over all speckle epochs.

Final star lists for the wide field mosaics require additional steps and a different treatment of the uncertainties. Star lists are created for each tile in the mosaics as done with the central 10″ AO data. The full mosaic star list is then constructed by sequentially stitching together the lists from each tile following a procedure similar to that in Anderson & van der Marel (2010). We begin by first transforming the stars' positions from the central tile to their positions in the Sgr A*-radio rest frame, in which ∼1200 stars down to a *K*-band limiting magnitude of $K_{\rm lim} \sim 16$ were measured over the central 22″ × 22″ in Yelda et al. (2010) and are updated here (see next section). We note that our wide field mosaics include fainter ($K_{\rm lim} \sim 18$) and more distant (FOV ∼ 30″ × 30″) stars than what was measured in Yelda et al. (2010). Once the central tile is transformed, a new reference list of positions is created in the following way. For stars that are matched, their positions and their associated errors are updated. The new positions are taken as the weighted average of the positions in the existing reference list and the transformed star list.[6] The new positional errors are taken as the average of the errors. For the stars that do not have positions in the Sgr A*-radio frame (i.e., those fainter than $K \sim 16$ or outside the 22″ × 22″ FOV), we include their transformed positions and their original errors (centroiding and distortion errors) in the new reference list. This new list then serves as the reference list for the stitching of the next tile in the sequence. This procedure is repeated until all tiles are aligned. After the central field from the nine-point dither observations is first aligned, the tiles from the four-point dither (if they were taken) are aligned (in the order: SW, NE, SE, NW). This is followed by the alignment of the remaining tiles from the nine-point dither observations (in the order: E, W, N, S, NE, SE, NW, SW). After completing the full alignment, we refine this intermediate star list by once again transforming each tile's star list to it a final time. In this instance, the averaging is done once all tiles are transformed and the intermediate reference list of positions is not included in the averaging. Each of the alignments performed in these

[5] We note that this step was done after the cross-epoch coordinate transformation discussed in Section 3.1.3.

[6] Distortion errors include the statistical error (∼0.05 pix) in the optical distortion model and the residual distortion term (∼0.1 pix), both of which are described in Yelda et al. (2010).

steps involves a second-order polynomial transformation, which consists of 12 coefficients.

3.1.3. Cross-epoch Coordinate Transformations

In order to measure relative positions and proper motions, stellar positions from each epoch must be transformed to a common reference coordinate system. This procedure is complicated by the fact that stars available for performing the transformation have detectable proper motions. Previous GC astrometric reference frames were constructed by minimizing the net displacement of reference stars between star lists, a procedure which implicitly assumes that these stars have no net motion over the field (the "cluster" reference frame; e.g., Eckart & Genzel 1997; Ghez et al. 1998, 2008; Gillessen et al. 2009).[7] However, net motion is known to exist in the GC, including an overall rotation of the late-type star cluster in the plane of the Galaxy (Trippe et al. 2008; Schödel et al. 2009; Yelda et al. 2010), as well as coherent motion in a CW, young stellar disk in the central parsec (Levin & Beloborodov 2003; Genzel et al. 2003; Paumard et al. 2006; Lu et al. 2009; Bartko et al. 2009). Neglecting to account for this motion results in degeneracies between the transformation parameters and the measured stellar velocities. It is therefore important to understand the motion of these stars if they are to be used in the construction of a stable reference frame.

The absolute positions and proper motions presented in Yelda et al. (2010) of >1200 GC stars offers an opportunity to construct a stable astrometric reference frame for this work. Astrometric measurements of these stars were determined relative to Sgr A* in a reference frame constructed by tying infrared astrometry of seven SiO masers to their precise radio measurements (the "maser" reference frame; Reid et al. 2007; Yelda et al. 2010). Here we update the positions and velocities of these "secondary" standards using a slightly modified version of the analysis described in Yelda et al. (2010). Specifically, we now use mosaicked star lists as opposed to mosaicked images. The nine tiles are stitched together in the following order: C, E, W, N, S, NE, SE, NW, SW. The final positions and their uncertainties are computed using a similar procedure as described in Section 3.1.2. The Sgr A*-rest reference frame was otherwise created in the same way as in Yelda et al. (2010). The updated positions and proper motions relative to Sgr A* for 1210 stars are presented in Appendix D.

The alignment of the stars' positions across all epochs is a multi-step process. The star lists from the deep central AO and speckle images are transformed to the coordinate system defined by the 2006 June AO image using a second-order polynomial transformation. This epoch was chosen as the reference epoch, $t_{\rm ref}$ because it is one of the deepest of our data sets ($K_{\rm lim}$ = 18.5 versus $K_{\rm lim}$ = 15.7 for our earlier fiducial epoch of 2004 July). In the alignment of each epoch, t_e, we first propagate the positions of the secondary astrometric standards from $t_{\rm ref}$ to the expected positions in t_e using their known absolute proper motions. We then find the best-fit transformation from the measured positions in t_e of the astrometric standard stars to their expected positions. This use of velocity information allows us to use all the astrometric standards, regardless of spectral type, and removes the degeneracy between frame transformations and the stellar velocities. Uncertainties from this transformation ($\sigma_{\rm aln}$) are characterized using a half-sample bootstrap. These alignment errors are a function of time from the reference epoch and of the number of reference stars used in the transformation. As seen in Figure 2, $\sigma_{\rm aln}$ is minimized near the reference epoch and is larger for the speckle epochs ($\sigma_{\rm aln}$ > 0.5 mas), which have on average ∼6× fewer reference stars than are available in AO epochs.

Given the high stellar density environment of the GC, it is important to consider the effects of source confusion (Ghez et al. 2008; Gillessen et al. 2009; Fritz et al. 2010). Stellar positions can be affected by unknown, underlying sources that have not previously been detected, or they may be affected by known sources that, when passing sufficiently close to a star, get detected as only one source instead of two. While it is not possible to account for the former case, we can determine when a star's positional measurement is biased by another known source. Using preliminary acceleration fits (see Section 3.1.4), the distance between every pair of stars in the narrow-field data is computed. For epochs in which the predicted positions of two stars come within 60 mas of one another (roughly the FWHM of our images), but only one star is actually detected, we exclude that detection as it is likely confused by the undetected source. Ten young stars (of the total 116) in this work were affected by confusion between 1 and 11 times, although IRS 16CC was confused in 26 epochs by a $K \sim 13$ mag star that has come within ∼30 mas since 2004. A total of 79 positional measurements were removed due to confusion, leaving 1756 positions for the narrow-field sources combined.

The mosaic star lists are aligned in a similar way as described above, but separately from the deep central and speckle data. The reference epoch chosen for the alignment of these three star lists was the 2008 observation, as this was the mid-point of these data sets. Young stars that are outside the central 10″ FOV and that are identified in all three mosaics are included in the orbital analysis. In other words, the astrometry obtained from the narrow field data sets takes precedence over the mosaic astrometry. The final analysis includes astrometry for 69 young stars from the central AO + speckle data sets and 47 young stars from the wide field mosaics, bringing the total number of young stars in this work to 116 and a total of 1897 positional measurements.

3.1.4. Proper Motion and Acceleration Measurements

All the x and y positions are independently fit as a function of time with kinematic models. For the central 10″ field, each star is fit with two models: (1) proper motion only and (2) proper motion and acceleration. Stars detected beyond the central 10″ field (i.e., those in the wide mosaic fields) have just three positional measurements and are therefore only fit for velocities. The reference time, t_0, for the position, velocity, and acceleration measurements of each star is chosen as the mean time of all epochs, weighted by the star's positional uncertainties. The velocity fits take on the form

$$x(t) = x_0 + v_{x,0}(t - t_0) \quad (1)$$

$$y(t) = y_0 + v_{y,0}(t - t_0), \quad (2)$$

and the acceleration fits are of the form

$$x(t) = x_0 + v_{x,0}(t - t_0) + \frac{1}{2}a_{x,0}(t - t_0)^2 \quad (3)$$

$$y(t) = y_0 + v_{y,0}(t - t_0) + \frac{1}{2}a_{y,0}(t - t_0)^2. \quad (4)$$

[7] We note that Gillessen et al. (2009) define a reference frame using a combination of the cluster and maser reference frames.

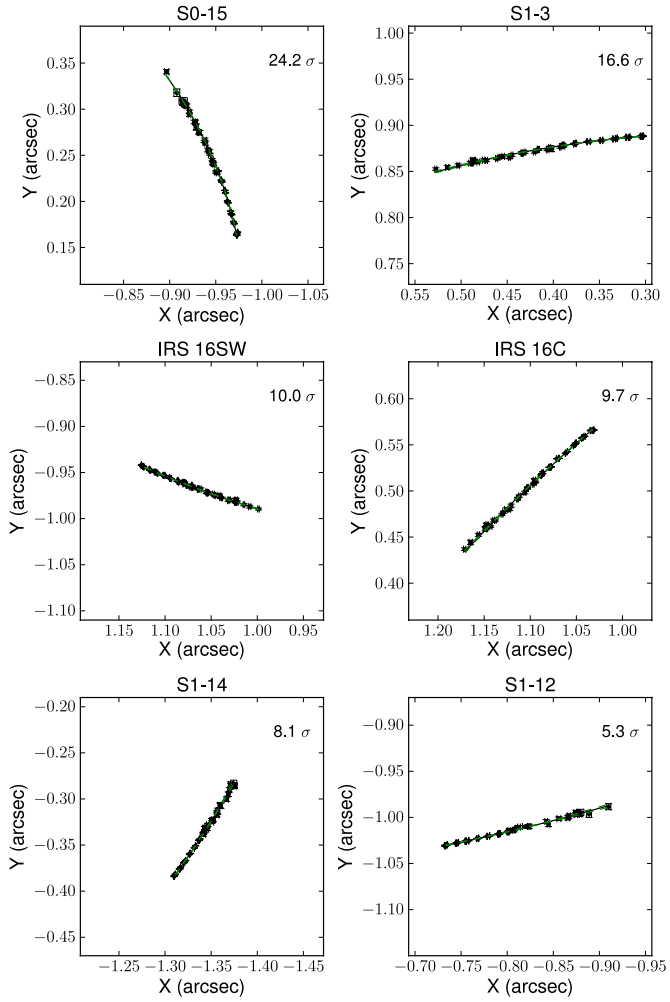

Figure 3. Positional measurements for the six stars beyond a projected radius of 0.″8 with reliable acceleration detections. Positions are measured relative to Sgr A*, with *X* and *Y* increasing to the East and North, respectively. Positional uncertainties do not include errors in the transformation to absolute coordinates (i.e., plate scale, location of Sgr A*, or position angle). The best-fit acceleration model is shown for each source (black solid) along with 1σ error bars (green dashed). The significance of each star's acceleration in the radial direction is shown in the upper right corner of each panel. The physical area is the same in each panel (0.″28 × 0.″28).

(A color version of this figure is available in the online journal.)

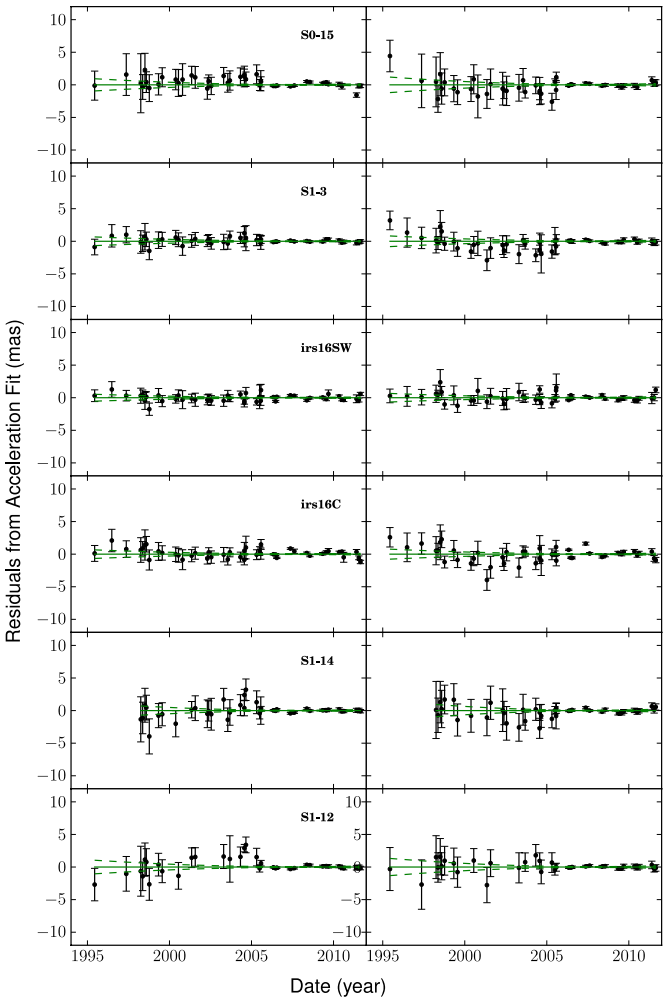

Figure 4. Residuals in X (left) and Y (right) after subtracting the best-fit acceleration curves shown in Figure 3 for each of the six accelerating sources.

(A color version of this figure is available in the online journal.)

Whether a star has measurable accelerated motion depends on several factors, including its distance from the SMBH, the time baseline over which it is detected, and the precision with which its positions are measured. To avoid including stars with non-physical accelerations, we require (1) the radial acceleration estimates to be significant at the $>5\sigma$ level ($N = 7$ stars) and (2) the tangential acceleration estimates to be insignificant at the $<5\sigma$ level, which eliminates one star.[8] With these criteria, we measure physical accelerations for the following six stars (beyond a projected radius of 0.″8): S0-15, S1-3, IRS 16C, S1-12, S1-14, IRS 16SW. The acceleration fits and residuals from the fits for these six stars are shown in Figures 3 and 4, respectively. This increases the number of acceleration measurements beyond 1″ over our previous work in Lu et al. (2009) by a factor of six, or equivalently, an additional five stars, three of which are reported by Gillessen et al. (2009). Furthermore, Gillessen et al. (2009) reports only one other physical acceleration from S1-2, which does not pass our criteria due to the large number of epochs in which it is affected by source confusion ($N = 15$ confused epochs). The most distant star from the SMBH for which an acceleration measurement is made is IRS 16SW, located at $R = 1.''5$ (~0.06 pc), which is well outside the inner edge of the stellar disk. For all other sources, the proper motion fit is used. We present the positions, proper motions, and accelerations for our sample in Table 4.

The position, proper motion, and acceleration uncertainties from the fitting procedure as a function of projected radius are shown in Figure 5. The smallest uncertainties are measured for stars with $R < 2.''5$, which are detected in both speckle and AO data sets and therefore have the longest time baseline. The observed increase in errors with radius is a result of alignment uncertainties and the number of epochs. For the central 10″ sources, the median errors in positions and proper motions are 0.05 mas and 0.03 mas yr^{-1}, respectively. The position and proper motion measurements of stars at large radii and detected in only the wide mosaics have typical uncertainties of 0.4 mas and 0.23 mas yr^{-1}, respectively. These relatively high

[8] This star, S1-8, shows a significant tangential acceleration (6σ) in our analysis, which we do not believe is real. We are in the process of implementing a new data reduction technique known as speckle holography (Schödel et al. 2013) on our speckle observations (instead of simple shift-and-add), and our preliminary analysis shows no significant non-physical accelerations.

Table 4
Kinematic Data of Galactic Center Young Stars

Name	K (mag)	N epochs	Epoch[a] (year)	ΔR.A. (arcsec)	$\sigma_{\rm R.A.}$ (mas)	ΔDecl. (arcsec)	$\sigma_{\rm Decl.}$ (mas)	$v_{\rm R.A.}$ (mas yr^{-1})	$v_{\rm Decl.}$ (mas yr^{-1})	v_z (km s^{-1})	v_z [b] Ref.	a_R [c] (mas yr^{-2})	Disk Prob. $(1-L)$
Stars with Acceleration Detections													
S1-3	12.1	45	2007.7	0.357	0.047	0.888	0.053	-13.70 ± 0.02	1.73 ± 0.03	-72 ± 38	1	-0.160 ± 0.010	0.415
S0-15	13.6	43	2007.6	-0.962	0.046	0.214	0.055	-3.47 ± 0.02	-10.82 ± 0.03	-597 ± 8	1	-0.293 ± 0.012	0.950
irs16C	9.8	45	2007.5	1.068	0.047	0.539	0.051	-8.54 ± 0.02	7.72 ± 0.02	158 ± 40	2	-0.083 ± 0.009	0.447
S1-12	13.7	36	2007.8	-0.777	0.047	-1.016	0.056	10.84 ± 0.02	-2.42 ± 0.03	-34 ± 30	1	-0.082 ± 0.015	0.487
S1-14	12.8	40	2007.8	-1.332	0.047	-0.349	0.056	4.96 ± 0.02	-7.39 ± 0.03	-364 ± 10	1	-0.123 ± 0.015	0.497
irs16SW	10.0	45	2007.3	1.091	0.046	-0.952	0.050	7.37 ± 0.02	2.97 ± 0.02	470 ± 50	2	-0.074 ± 0.007	0.082
Linearly Moving Stars with Acceleration Constraints													
S0-14	13.7	36	2007.9	-0.764	0.047	-0.277	0.063	2.16 ± 0.02	-0.93 ± 0.03	-16 ± 9	1	> -0.120	0.011
S1-1	13.0	45	2007.7	1.027	0.046	0.037	0.052	5.62 ± 0.02	1.62 ± 0.03	536 ± 30	2	> -0.025	0.000
irs16NW	10.1	45	2007.6	0.064	0.044	1.223	0.051	5.79 ± 0.02	1.21 ± 0.03	-15 ± 50	2	> -0.045	0.000
S1-33	14.9	35	2008.0	-1.246	0.051	-0.007	0.065	-0.34 ± 0.02	5.55 ± 0.03	3 ± 17	1	> -0.110	0.000
S1-18	14.9	43	2007.8	-0.773	0.050	1.508	0.058	-7.63 ± 0.02	1.13 ± 0.03	-249 ± 50	1	> -0.050	0.022
S1-22	12.7	32	2007.8	-1.588	0.049	-0.509	0.060	7.73 ± 0.02	-2.60 ± 0.03	-235 ± 100	2	> -0.122	0.201
S2-4	12.2	35	2007.6	1.498	0.045	-1.459	0.048	7.94 ± 0.02	3.07 ± 0.03	208 ± 29	1	> -0.023	0.205
S2-7	14.1	42	2007.7	0.943	0.045	1.853	0.053	-6.61 ± 0.02	1.83 ± 0.03	-94 ± 50	3	> -0.053	0.228
S2-6	12.0	38	2007.6	1.641	0.044	-1.332	0.048	7.85 ± 0.02	2.33 ± 0.02	148 ± 29	1	> -0.020	0.068
irs16SW-E	11.0	39	2007.6	1.880	0.042	-1.120	0.047	5.87 ± 0.02	3.89 ± 0.02	366 ± 70	2, 3	> -0.028	0.047
S2-22	12.9	44	2007.7	2.304	0.044	-0.214	0.048	-1.63 ± 0.02	6.42 ± 0.02	49 ± 50	2	> -0.040	0.000
S2-58	14.0	37	2007.9	2.146	0.053	-1.134	0.052	-0.73 ± 0.02	6.62 ± 0.03	63 ± 32	1	> -0.040	0.000
Linearly Moving Stars													
S1-2	14.7	30	2007.8	0.046	0.045	-1.011	0.054	13.10 ± 0.02	-0.12 ± 0.03	34 ± 30	1		0.286
S1-8	14.1	41	2007.7	-0.606	0.042	-0.898	0.050	9.05 ± 0.02	-5.24 ± 0.03	-171 ± 10	1		0.500
S1-21	13.3	27	2007.9	-1.650	0.042	0.109	0.051	4.02 ± 0.02	-4.79 ± 0.03	-29 ± 70	1		0.132
S1-19	13.6	29	2007.7	0.411	0.042	-1.623	0.050	8.41 ± 0.02	-3.11 ± 0.03	-164 ± 30	1		0.205
S1-24	11.5	30	2007.7	0.728	0.042	-1.631	0.048	2.64 ± 0.02	-6.16 ± 0.03	116 ± 36	1		0.000
irs16CC	10.6	19	2001.3	1.997	0.263	0.545	0.292	-1.72 ± 0.11	6.79 ± 0.11	241 ± 25	2, 3		0.391
irs29N	10.4	17	2009.0	-1.560	0.051	1.381	0.069	4.75 ± 0.04	-5.05 ± 0.05	-190 ± 90	2, 3		0.034
irs33N	11.2	20	2007.8	-0.037	0.041	-2.222	0.052	3.62 ± 0.02	-5.54 ± 0.03	20 ± 14	1		0.000
S2-50	15.3	24	2008.1	1.696	0.069	-1.503	0.074	2.25 ± 0.04	2.22 ± 0.04	-56 ± 122	1		0.275
S2-17	10.8	25	2007.9	1.323	0.041	-1.871	0.048	9.24 ± 0.02	0.15 ± 0.03	62 ± 10	1		0.296
S2-16	11.9	23	2008.0	-1.052	0.041	2.066	0.051	-9.16 ± 0.02	-0.61 ± 0.03	-100 ± 70	2, 3		0.730
S2-21	13.4	20	2007.8	-1.641	0.042	-1.658	0.055	9.35 ± 0.03	-3.33 ± 0.04	-109 ± 39	1		0.476
S2-19	12.6	24	2007.8	0.398	0.043	2.311	0.050	-8.28 ± 0.02	1.32 ± 0.03	41 ± 20	2, 3		0.346
S2-74	13.1	19	2007.8	0.134	0.045	2.781	0.054	-8.84 ± 0.03	1.55 ± 0.03	36 ± 20	2, 3		0.276
S2-76	15.4	9	2010.2	-0.225	0.090	2.811	0.116	2.81 ± 0.12	1.86 ± 0.15	-28 ± 73	1		0.000
irs16NE	9.1	26	2008.0	2.888	0.052	0.981	0.058	3.05 ± 0.03	-8.90 ± 0.04	-10 ± 20	2, 3		0.000
S3-2	12.0	24	2007.9	3.076	0.041	0.555	0.049	4.31 ± 0.02	1.30 ± 0.03	-446 ± 23	1		0.000
S3-3	15.0	22	2008.1	3.082	0.040	-0.645	0.051	3.76 ± 0.02	4.57 ± 0.03	43 ± 30	1		0.000
S3-5	12.0	22	2008.0	2.953	0.038	-1.153	0.044	2.87 ± 0.02	4.94 ± 0.03	327 ± 100	2, 3		0.430
S3-96	14.4	17	2008.9	-3.133	0.068	-0.627	0.090	-0.07 ± 0.04	5.64 ± 0.06	40 ± 40	2, 3		0.000
S3-19	11.9	19	2007.9	-1.566	0.043	-2.786	0.055	7.90 ± 0.03	-1.30 ± 0.04	-114 ± 50	2, 3		0.317
irs33E	10.2	19	2008.0	0.691	0.041	-3.127	0.055	6.85 ± 0.02	-1.06 ± 0.04	170 ± 20	2, 3		0.026
S3-25	13.9	19	2007.6	1.424	0.046	2.959	0.054	-7.08 ± 0.03	0.77 ± 0.04	-84 ± 6	2		0.195
S3-26	12.3	19	2007.8	-2.588	0.045	-2.069	0.056	5.80 ± 0.03	2.12 ± 0.04	63 ± 30	2, 3		0.085
S3-30	12.4	19	2008.0	1.661	0.039	-2.937	0.049	-0.72 ± 0.02	4.32 ± 0.03	0 ± 90	1		0.018
irs13E1	10.6	19	2007.8	-2.971	0.046	-1.647	0.056	-3.87 ± 0.03	-1.98 ± 0.04	-3 ± 11	1		0.000
S3-190	14.0	19	2008.2	-3.186	0.048	1.423	0.058	-3.27 ± 0.03	-2.29 ± 0.04	-244 ± 80	1		0.215
S3-10	12.1	19	2008.0	3.340	0.039	-1.113	0.045	-0.14 ± 0.02	5.50 ± 0.03	305 ± 70	2		0.427
irs13E4	11.8	19	2008.1	-3.231	0.303	-1.403	0.294	-5.77 ± 0.17	1.70 ± 0.14	56 ± 70	2, 3		0.000
irs13E2	10.6	19	2007.7	-3.190	0.047	-1.726	0.057	-6.78 ± 0.03	1.43 ± 0.04	40 ± 40	2, 3		0.000
S3-314	15.3	19	2007.9	3.829	0.045	-0.090	0.058	3.08 ± 0.03	4.16 ± 0.04	11 ± 17	1		0.000
S3-331	13.6	19	2008.0	-1.238	0.060	3.650	0.084	5.70 ± 0.04	4.64 ± 0.05	-167 ± 20	2, 3		0.000
S3-374	12.3	19	2007.7	-2.757	0.046	-2.835	0.056	-0.49 ± 0.03	-3.78 ± 0.04	20 ± 20	2		0.000
S4-36	12.6	19	2007.8	-3.685	0.056	1.794	0.063	-5.37 ± 0.03	-3.92 ± 0.04	-154 ± 25	2, 3		0.345
S4-71	12.3	18	2008.0	0.769	0.040	-4.076	0.056	0.12 ± 0.02	-4.28 ± 0.04	60 ± 50	2		0.000
irs34W	11.6	19	2007.9	-4.066	0.059	1.570	0.063	-2.66 ± 0.04	-4.89 ± 0.04	-290 ± 30	2, 3		0.441
S4-169	13.5	18	2007.8	4.417	0.046	0.274	0.066	-2.28 ± 0.03	4.42 ± 0.05	145 ± 51	1		0.555
irs3E	11.4	19	2007.8	-2.338	0.064	3.816	0.081	4.61 ± 0.04	1.19 ± 0.05	107 ± 100	3		0.000
irs7SE	13.3	19	2007.3	2.976	0.051	3.469	0.062	5.84 ± 0.04	0.22 ± 0.05	-150 ± 100	2, 3		0.000
S4-258	12.6	19	2007.5	-4.392	0.062	-1.630	0.062	-4.70 ± 0.04	2.45 ± 0.05	330 ± 80	2, 3		0.000
S4-262	15.9	17	2008.1	4.280	0.048	-1.939	0.069	-1.25 ± 0.03	-5.09 ± 0.05	43 ± 64	1		0.000
irs34NW	13.2	16	2007.7	-3.766	0.062	2.839	0.070	-5.94 ± 0.04	-3.33 ± 0.05	-150 ± 30	2, 3		0.519

Table 4
(Continued)

Name	K (mag)	N epochs	Epoch[a] (year)	ΔR.A. (arcsec)	$\sigma_{\rm R.A.}$ (mas)	ΔDecl. (arcsec)	$\sigma_{\rm Decl.}$ (mas)	$v_{\rm R.A.}$ (mas yr^{-1})	$v_{\rm Decl.}$ (mas yr^{-1})	v_z (km s^{-1})	v_z [b] Ref.	a_R [c] (mas yr^{-2})	Disk Prob. ($1-L$)
S4-287	13.6	17	2007.8	0.125	0.041	−4.767	0.059	2.97 ± 0.02	1.57 ± 0.04	-51 ± 65	1		0.058
S4-364	11.7	3	2007.8	2.224	0.380	4.481	0.355	5.77 ± 0.20	-2.30 ± 0.22	-134 ± 40	2, 3		0.000
S5-34	13.6	19	2007.6	−4.329	0.073	−2.731	0.070	-3.61 ± 0.04	-1.68 ± 0.05	-40 ± 70	2		0.000
irs1W	10.9	15	2008.3	5.255	0.455	0.620	1.372	-1.35 ± 0.21	9.66 ± 0.74	-36 ± 32	1		0.000
S5-235	13.2	3	2007.8	2.781	0.391	4.553	0.381	-1.14 ± 0.20	-3.77 ± 0.22	-115 ± 50	2		0.000
S5-237	13.2	3	2007.8	5.500	0.403	1.002	0.361	-1.33 ± 0.23	6.44 ± 0.18	35 ± 17	1		0.000
S5-236	13.1	3	2008.4	−5.547	0.442	−1.282	0.433	4.43 ± 0.22	1.95 ± 0.21	155 ± 50	2		0.000
S5-183	11.5	17	2007.4	4.604	0.048	−3.431	0.061	-4.29 ± 0.03	-1.90 ± 0.05	-148 ± 16	1		0.000
S5-187	13.2	17	2007.5	−1.712	0.053	−5.532	0.071	-0.97 ± 0.03	-3.76 ± 0.05	10 ± 50	2		0.000
S5-231	12.0	3	2008.4	5.813	0.848	0.097	0.343	0.02 ± 0.56	6.04 ± 0.17	24 ± 25	2		0.000
S5-191	12.8	17	2007.9	3.184	0.051	−4.872	0.073	-1.35 ± 0.03	-3.54 ± 0.05	140 ± 50	2		0.000
S6-89	12.1	16	2009.2	5.445	0.225	3.013	0.272	3.05 ± 0.16	-6.01 ± 0.16	-135 ± 70	2		0.000
irs9W	12.1	17	2007.4	2.882	0.051	−5.593	0.077	5.62 ± 0.03	3.58 ± 0.06	140 ± 50	2, 3		0.422
S6-90	12.3	3	2007.9	−3.954	0.408	4.924	0.405	-0.50 ± 0.24	-2.93 ± 0.23	-350 ± 50	2, 3		0.005
S6-96	12.8	3	2006.9	−6.045	0.563	−1.940	0.688	-1.35 ± 0.37	8.38 ± 0.57	-35 ± 50	2		0.000
S6-81	11.0	3	2008.1	6.360	0.348	0.267	0.290	-2.16 ± 0.20	5.34 ± 0.15	-14 ± 13	1		0.000
S6-95	13.2	3	2008.1	−2.420	0.411	6.004	0.410	4.02 ± 0.22	0.77 ± 0.22	-305 ± 100	2, 3		0.000
S6-63	11.2	17	2007.9	1.852	0.074	−6.306	0.172	6.04 ± 0.05	1.80 ± 0.09	110 ± 50	2		0.611
S6-93	12.8	3	2008.1	4.448	0.396	4.973	0.369	4.69 ± 0.21	-0.85 ± 0.20	-80 ± 100	2, 3		0.000
S6-100	13.9	3	2008.0	1.562	0.418	6.524	0.419	-4.87 ± 0.22	2.87 ± 0.20	-300 ± 150	3		0.016
S6-82	13.5	3	2007.5	6.715	0.401	−0.470	0.412	2.07 ± 0.19	5.68 ± 0.26	86 ± 100	2, 3		0.184
S7-30	13.9	3	2008.4	6.469	0.332	−2.682	0.287	-2.63 ± 0.19	-3.32 ± 0.15	-87 ± 90	1		0.000
S7-161	13.6	3	2009.5	−7.376	0.605	0.061	0.599	-2.16 ± 0.49	-2.55 ± 0.40	-120 ± 50	2		0.333
S7-16	12.5	3	2008.1	1.621	0.358	−7.236	0.354	2.49 ± 0.21	3.30 ± 0.23	160 ± 50	2		0.264
S7-19	13.2	3	2007.8	−3.794	0.411	6.507	0.372	4.22 ± 0.24	3.52 ± 0.19	-65 ± 50	2		0.000
S7-180	13.4	3	2008.9	−7.360	0.558	−1.637	0.580	-3.92 ± 0.28	0.48 ± 0.29	120 ± 70	2		0.000
S7-10	11.4	3	2008.1	−1.105	0.399	7.635	0.338	-5.14 ± 0.19	-1.87 ± 0.16	-92 ± 40	2, 3		0.474
S7-36	14.4	3	2008.5	6.363	0.376	−4.415	0.309	2.63 ± 0.20	2.33 ± 0.16	26 ± 46	1		0.180
S7-216	10.7	3	2008.4	−7.731	0.449	1.424	0.413	1.82 ± 0.24	6.59 ± 0.23	60 ± 50	2		0.000
S7-20	13.3	3	2008.4	−3.700	0.474	6.955	0.490	4.11 ± 0.26	2.89 ± 0.26	-45 ± 50	2		0.000
S7-228	11.8	3	2008.3	−7.741	0.477	1.708	0.432	2.19 ± 0.26	3.67 ± 0.23	150 ± 30	2		0.000
S7-236	12.5	3	2007.7	−7.093	0.451	3.598	0.393	-3.65 ± 0.28	-2.59 ± 0.25	-170 ± 70	2		0.681
S8-15	13.0	3	2008.2	−1.603	0.343	8.043	0.270	-3.30 ± 0.20	-2.64 ± 0.16	-130 ± 50	2		0.387
S8-7	11.9	3	2008.3	−3.688	0.397	−7.415	0.345	4.53 ± 0.20	0.54 ± 0.19	30 ± 100	2		0.516
S8-181	11.6	3	2007.9	−7.620	0.393	−3.580	0.374	-2.15 ± 0.24	-1.90 ± 0.20	70 ± 70	2, 3		0.005
S8-4	11.0	3	2008.3	−0.021	0.324	8.560	0.263	-0.92 ± 0.18	3.81 ± 0.16	-138 ± 40	2, 3		0.000
S8-196	12.4	3	2008.4	−8.087	0.426	−2.896	0.371	0.16 ± 0.26	-0.14 ± 0.21	190 ± 50	2		0.000
S9-143	12.6	3	2008.1	−8.365	0.416	−3.347	0.380	-0.33 ± 0.25	-1.29 ± 0.21	40 ± 100	2		0.112
S9-20	13.2	3	2007.8	4.304	0.490	−8.031	0.388	2.55 ± 0.27	1.48 ± 0.21	180 ± 80	2, 3		0.227
S9-23	13.6	3	2008.2	−1.277	0.342	9.151	0.285	-3.89 ± 0.18	-3.43 ± 0.17	-185 ± 50	2		0.156
S9-13	13.1	3	2008.2	−3.019	0.360	8.821	0.334	2.00 ± 0.19	3.68 ± 0.20	-160 ± 50	2		0.000
S9-1	12.6	3	2008.4	9.450	0.321	0.281	0.265	-1.79 ± 0.18	-2.59 ± 0.16	-230 ± 100	2, 3		0.000
S9-114	10.8	3	2008.3	−6.509	0.341	−6.886	0.308	2.08 ± 0.20	3.22 ± 0.18	160 ± 50	2		0.000
S9-283	12.5	3	2008.1	−9.605	0.368	−2.539	0.335	0.80 ± 0.23	1.00 ± 0.21	30 ± 70	2, 3		0.000
S9-9	11.7	3	2008.4	5.650	0.329	−8.182	0.323	-0.91 ± 0.18	-1.18 ± 0.17	130 ± 100	2, 3		0.000
S10-50	14.7	3	2008.2	9.586	0.386	−3.160	0.314	-0.48 ± 0.21	-3.88 ± 0.16	96 ± 87	1		0.000
S10-136	13.0	3	2007.9	−8.624	0.488	−5.289	0.469	-1.76 ± 0.27	6.04 ± 0.26	-70 ± 70	2, 3		0.000
S10-5	11.9	3	2008.3	−1.574	0.347	10.039	0.355	-1.67 ± 0.18	-1.18 ± 0.21	-180 ± 70	2, 3		0.047
S10-4	11.2	3	2008.1	0.078	0.351	10.254	0.347	-2.09 ± 0.19	1.56 ± 0.21	-250 ± 40	2, 3		0.000
S10-32	14.4	3	2008.3	10.200	0.354	−1.694	0.317	3.41 ± 0.18	3.68 ± 0.16	161 ± 27	1		0.366
S10-34	14.5	3	2008.4	8.877	0.483	−5.626	0.485	1.08 ± 0.23	3.76 ± 0.24	-107 ± 135	1		0.059
S10-7	12.7	3	2008.0	9.709	0.332	4.428	0.372	-0.34 ± 0.21	-4.24 ± 0.20	-150 ± 40	2, 3		0.000
S10-48	15.1	3	2007.2	−0.533	0.486	10.732	0.596	2.01 ± 0.22	1.56 ± 0.44	-205 ± 50	3		0.000
S11-21	13.5	3	2008.0	2.566	0.378	10.947	0.353	-2.08 ± 0.22	-1.78 ± 0.24	-160 ± 70	2		0.075
S11-5	11.9	3	2007.9	1.370	0.367	11.693	0.421	-0.26 ± 0.21	2.64 ± 0.30	-65 ± 40	2, 3		0.000
S13-3	11.9	3	2008.3	11.895	0.347	5.932	0.337	1.31 ± 0.20	2.28 ± 0.19	-190 ± 40	3		0.000

Notes. All uncertainties are 1σ relative errors and do not include errors in the plate scale, location of Sgr A*, or position angle.

[a] Epoch taken as the mean of the imaging observations, weighted by positional uncertainties for each star.

[b] Radial velocity data obtained from observations in (1) Do et al. (2009, 2013), (2) Bartko et al. (2009), and (3) Paumard et al. (2006). Note that some RV measurements reported in Bartko et al. (2009) were first reported in Paumard et al. (2006).

[c] Accelerations were fit for stars falling within the central 10″ field of view only. For stars with acceleration limits, the positions and velocities are from the linear fits and the acceleration limits are from the acceleration fits.

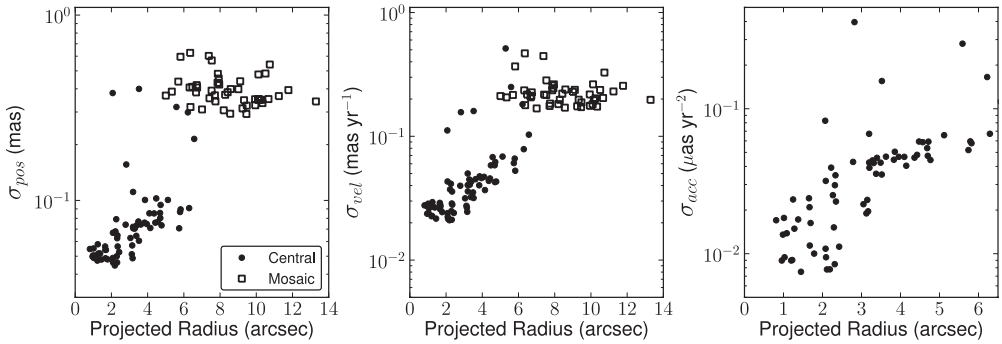

Figure 5. Observed position (left), proper motion (middle), and acceleration (right) uncertainties as a function of projected radius. The average uncertainty along the *X* and *Y* coordinates are plotted. The filled circles mark the stars in our narrow-field data set and unfilled squares indicate the stars in the wide-field mosaic data, which have projected radii $R > 5''$.

uncertainties are a result of having only three measurements and a four-year baseline. We also show the astrometric uncertainties as a function of *K* magnitude and number of epochs for stars in the central 10″ data set in Figure 6. The figure shows that the uncertainties have little dependence on magnitude but strongly correlate with the number of epochs a star is detected in. Acceleration uncertainties for the 6 stars with reliable acceleration measurements and the 12 stars with 3σ acceleration upper limits (see below) are highlighted in the bottom panel of Figure 6. The average acceleration uncertainty among 18 these stars is 10 μas yr^{-2} ($\sim$0.4 km s^{-1} yr^{-1}), which is a factor of six improvement over our earlier efforts in Lu et al. (2009). These measurements match and sometimes exceed the highest astrometric precision that has been reported to date (Gillessen et al. 2009). For completeness, we show the RV uncertainties for all 116 young stars in the sample and indicate the source of the measurement that we use in our analysis (i.e., Keck/OSIRIS or VLT/SINFONI).

3.2. Radial Velocities

Each OSIRIS RV estimate is made by fitting a Gaussian model to the Brγ line profile and comparing the wavelength of the best-fit peak to the rest wavelength of $\lambda_0 = 2.1661$ μm. The velocities are then transformed to the local standard of rest (LSR) reference frame by correcting for the Earth's rotation and motion around the sun, and for the Sun's peculiar motion. RV uncertainties ($\sigma_{\rm RV}$) from OSIRIS are estimated as the rms of the line profile fits from three independent subsets of the original data and range from $\sim$10 to 90 km s^{-1} ($\langle\sigma_{\rm RV}\rangle = 42$ km s^{-1}). For the star S1-24 ($K = 11.5$), however, only a single frame was obtained, which had an S/N = 74. Given this relatively high S/N, we choose to include this RV measurement and we estimate its uncertainty using an empirically derived relation between S/N and $\sigma_{\rm RV}$:

$$\sigma_{\rm RV} = 175.4 \times {\rm S/N}^{-0.367}. \quad (5)$$

Further details on the RV extraction process are reported in Ghez et al. (2008). The RV values and their uncertainties are reported in Table 4.

If multiple RV measurements for a star exist, the Keck measurements take precedence, followed by the Very Large Telescope (VLT) measurements reported in Bartko et al. (2009) and Paumard et al. (2006). This results in a sample of RV measurements, of which 38 were made with OSIRIS and 78 were taken from either Bartko et al. (2009) or Paumard et al. (2006) ($\langle\sigma_{\rm RV}\rangle = 57$ km s^{-1}). The 15 stars that are in common between the Do et al. OSIRIS observations and the VLT observations are shown in the right panel of Figure 7, and the measurements between the two telescopes are consistent within their uncertainties except for IRS 13E1. Using the VLT RVs for

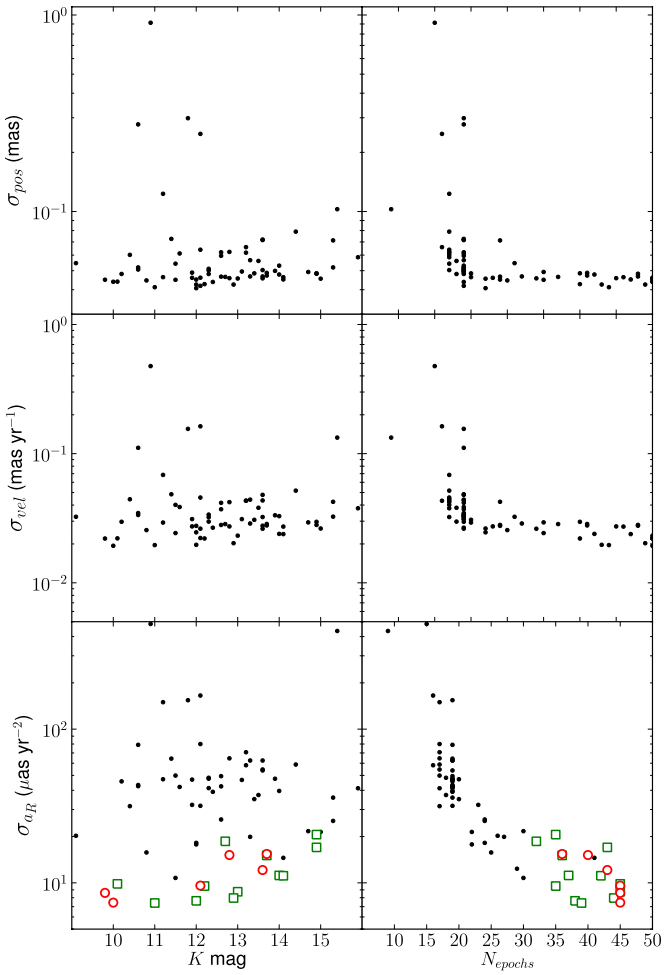

Figure 6. Position (top), proper motion (middle), and radial acceleration (bottom) uncertainties as a function of *K* magnitude (left) and number of epochs (right) for our sample of young stars beyond a projected radius of 0.″8 and in the central 10″ AO data set. Note that the acceleration uncertainties are shown in μas yr^{-2}. The astrometric uncertainties are estimated from either the proper motion or acceleration fit to each star's individual positions over time. Stars with acceleration detections and acceleration constraints are shown as open red circles and open green squares, respectively. The figures show that our astrometric uncertainties have only a slight dependence on stellar magnitudes and a strong dependence on the number of epochs a star was detected in.

(A color version of this figure is available in the online journal.)

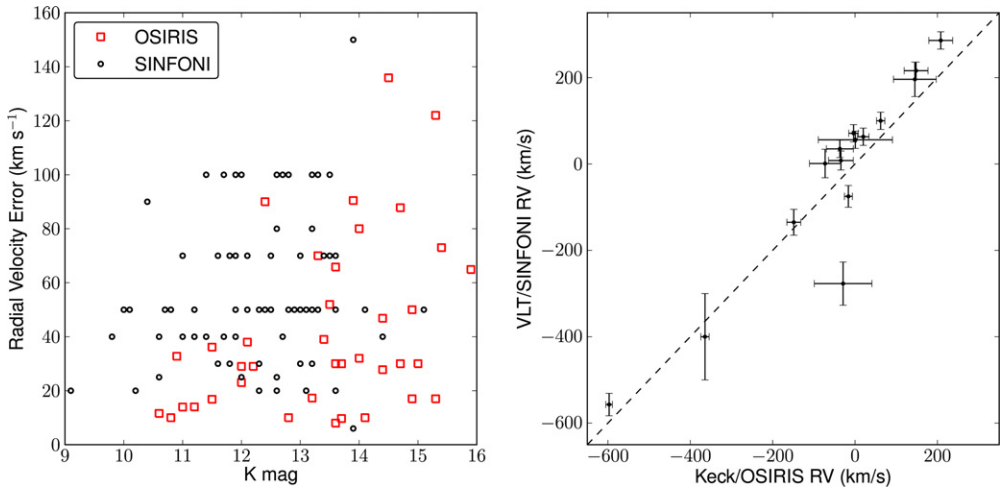

Figure 7. Left: line-of-sight velocity uncertainties plotted against K magnitude for the Keck/OSIRIS (red squares) and VLT/SINFONI (black circles) measurements. Right: comparison of radial velocity measurements for the 15 common stars in the two data sets.

(A color version of this figure is available in the online journal.)

these 15 stars does not change the results presented here. The Do et al. (2013) observations were designed to sample the eastern portion of the CW disk in order to maximize the number of young star identifications. With observed K magnitudes ranging from ∼10 to 16, the Do et al. samples include O stars at the bright end and B1V stars at the faint end. In contrast, Bartko et al. (2009) include mainly WR and O-type stars ($K < 14$), all 90 of which are included in our sample. The uncertainties in the RV measurements from both OSIRIS and SINFONI are shown in Figure 7. We note that there was no attempt to extract RVs of the bright WR stars from the OSIRIS data.

3.3. Orbital Analysis

With six kinematic variables measured (x_0, y_0, z, v_x, v_y, v_z, a_R), the standard Keplerian orbital elements (inclination i, angle to the ascending node Ω, time of periapse passage T_0, longitude of periapse ω, period P, and eccentricity e) can be estimated if the central potential is known (see Lu et al. 2009 Appendix B for conversion equations). The description of the central potential used in this analysis is based on a spherically symmetric mass, $M_{\rm tot}$, located at a distance R_0, and composed of the mass of the central SMBH, $M_{\rm BH}$, and an extended mass component from the nuclear star cluster, $M_{\rm ext}$. In this work, we rederive the $M_{\rm BH}$ and R_0 from the orbit of the 16 yr period central-arcsecond star, S0-2, using (1) the astrometry from the aligned star lists reported here to ensure that the position of Sgr A* is identified in the same reference frame as our stellar kinematic measurements, and (2) all RVs used by Ghez et al. (2008) and newly acquired data from OSIRIS since that work;[9] this results in an $M_{\rm BH}$ estimate of $4.6 \pm 0.7 \times 10^6$ $M_\odot$ and an R_0 estimate of 8.23 ± 0.67 kpc. We base $M_{\rm ext}$ on the work of Schödel et al. (2009) and take it to be $M_{\rm ext}(r = 1\ {\rm pc}) \sim 1 \pm 0.4 \times 10^6$ $M_\odot$, where the error is the difference in extended mass estimates from their isotropic and anisotropic velocity models. If $M_{\rm ext}$ is modeled as

$$M_{\rm ext} = 4\pi \int \rho(r) r^2 dr, \tag{6}$$

where the mass density, $\rho(r)$, is a power-law of the form

$$\rho(r) = \rho_0 \left(\frac{r}{5\ {\rm pc}} \right)^{-1}, \tag{7}$$

then $\rho_0 = 3.2 \pm 1.3 \times 10^4$ $M_\odot$ pc^{-3}. For the radial range of our data (assuming $z = 0$), this leads to $M_{\rm ext} < 5 \times 10^5$ $M_\odot$, which is an order of magnitude smaller than the mass of the SMBH and should therefore have a minimal effect on the orbital estimates, but we include it for completeness.

Our orbital analysis breaks down into the following three categories based on the information content contained in the acceleration measurement: (1) stars with significant acceleration detections ($N = 6$), (2) stars with acceleration upper limits below or equivalent to the nominal theoretical maximum acceleration and for which a lower limit to the line-of-sight distance can be estimated (i.e., inferred from the lack of acceleration; $N = 12$), and (3) all other stars ($N = 98$). Stars with acceleration detections and with useful upper limits are shown in Figure 8. For stars that show significant deviations from linear motion in the plane of the sky, the measured a_R is converted to a line-of-sight distance through the following relationship:

$$a_R = \frac{-G M_{\rm tot}(r) R}{r^3} \simeq \frac{-G M_{\rm tot}(R) R}{(R^2 + z^2)^{3/2}}. \tag{8}$$

While we do not know the line-of-sight distance (and therefore the full 3D distance) a priori, we use the star's projected radius (R) as the star's 3D radius (r) to determine $M_{\rm ext}$, which is a lower limit on the true extended mass. This allows Equation (8) to be rearranged to obtain z,

$$|z| = \left[\left(\frac{G M_{\rm tot}(R) R}{a_R} \right)^{2/3} - R^2 \right]^{1/2}. \tag{9}$$

We note that there is a sign ambiguity in the line-of-sight distance, which results in degenerate orbital solutions.

With two possible z solutions in hand, two sets of orbital elements are found. The probability density functions (PDFs) for each are constructed by carrying out a Monte Carlo (MC) simulation in which 10^5 artificial data sets are created. In each data set, we sample the six kinematic measurements from Gaussian

[9] Since the analysis presented here was carried out, the black hole properties were rederived after including the most recent imaging observation from Keck in 2012 May as well as all currently published RV data (Meyer et al. 2012). The newly derived black hole mass and distance are consistent with the values we use to within 1σ.

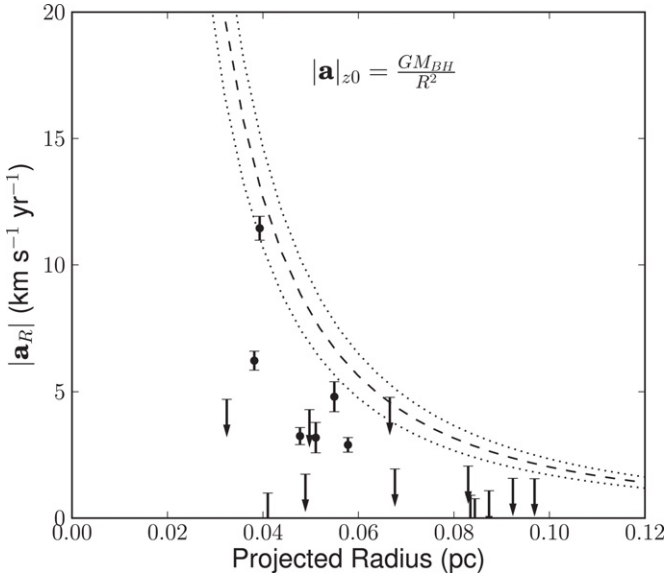

Figure 8. Accelerations along the radial coordinate as a function of the stars' projected radius, assuming $R_0 = 8.23$ kpc. The theoretical maximum acceleration ($|a|_{z0}$) for the nominal black hole mass of 4.6×10^6 $M_\odot$ is shown as the dashed curve, with the 1σ upper and lower boundaries shown as dotted curves. We detect six significant accelerations out to R = 1.″5 (0.06 pc), shown with 1σ error bars. These sources have known line-of-sight distances and therefore have the best determined orbital solutions. Stars with 3σ acceleration upper limits below the theoretical maximum acceleration are shown as downward pointing arrows and have strong constraints on their line-of-sight distances.

distributions, which have a mean and 1σ width corresponding to the variables' measured values and uncertainties. The gravitational potential parameters, $M_{\rm BH}$, R_0, x_0, and y_0, are sampled from a four-dimensional PDF based on the orbit of S0-2, and ρ_0 is sampled from a Gaussian distribution centered on the value quoted above. We note that in a given trial, all stars' orbits are determined using the same gravitational potential. Figure 9 shows the e, i, and Ω PDFs as a function of z for the six accelerating sources. The PDFs are constrained to small regions of parameter space for positive and negative z. Each of the degenerate sets of solutions have 1σ widths in i and Ω of less than 7° and in eccentricity of less than 0.14 for each of these stars.

Accelerations that are consistent with zero can also provide constraints on the line-of-sight distance. The maximum acceleration a star can have is $|a|_{z0} = GM_{\rm tot}(R)/R^2$, which is equivalent to the acceleration the star would have if its line-of-sight distance were $z = 0$. A star with a 3σ acceleration upper limit, $|a|_{3\sigma}$, that is less than $|a|_{z0}$ must therefore have a three-dimensional (3D) position that is larger than its observed projected position (i.e., $|z| > |z(a_{3\sigma})|$). Thus, the non-detection of an acceleration translates to a lower limit on the line-of-sight distance. Furthermore, the minimum acceleration allowed, $|a|_{\rm bound}$, is set by the assumption that the star is bound. For stars with 3σ upper limits below $|a|_{z0}$, we carry out the simulations similarly to those above, with the exception that we sample from a uniform acceleration distribution between $a_{\rm bound}$ and $a_{3\sigma}$. For all other stars, including those outside the central 10″ field (i.e., stars from the mosaic fields), we sample from a uniform acceleration distribution between $a_{\rm bound}$ and a_{z0}.

4. RESULTS

Compared to our earlier efforts in Lu et al. (2009), we have increased (1) the radial extent of our observations from 3″ to 13.″3, (2) the number of young stars in our sample from 32 to 116, (3) the number of reliable acceleration detections from 1 to 6, and (4) the number of useful acceleration upper limits (which constrain the orbital parameters) from 7 to 12. Taken together, these improvements provide tighter constraints on the orbits of the young stars as well as any kinematic structures present. We construct various ensemble distributions from the real data in Section 4.1. We also incorporate simulations of mock data sets, which are run through our orbital analysis and combined into the same distribution functions. The results are compared to the real data in order to model the true underlying distributions and to explore any biases introduced by measurement uncertainties and assumptions in our analyses (Section 4.2).

4.1. Observed Global Kinematic Structures

Kinematic structures are identified by constructing a density map of the normal vectors to the stars' orbital planes. The direction of the normal vector is described by inclination, i, and the P.A. of the ascending node, Ω. The density at each location (in stars deg^{-2}) in the PDF (i, Ω) map is computed for the six nearest normal vectors within a given trial in the MC simulation (Lu et al. 2009). These values are then averaged over all 10^5 MC trials to produce an average density map. Figure 10 shows the density map for all 116 stars in our observed sample using the HEALpix framework ($N_{\rm pixels} = 49152$ equal-area pixels; Górski et al. 2005). A clear peak of 0.024 stars deg^{-2} is found at (i, Ω) = (130°, 96°) and the half-width at half-maximum (HWHM) from the peak density is 15°. This peak corresponds to the CW disk reported in many earlier publications, including the original work by Levin & Beloborodov (2003). The direction of the disk plane differs by 15° ($\sim3\sigma$) from that in Lu et al. (2009) due to our use of an improved model for the optical distortion in our images (Yelda et al. 2010) and is within 1σ agreement with Paumard et al. (2006) and Bartko et al. (2009).

While the existence of the CW disk has been well-established prior to this work, it is important to estimate disk membership probabilities for each star in order to properly characterize the disk properties. The probabilities are calculated following Lu et al. (2009) and are $1 - L_{\rm non\text{-}disk}$, where $L_{\rm non\text{-}disk}$ is the likelihood that the star is not part of the disk, and is computed as

$$L_{\rm non\text{-}disk} = 1 - \frac{\int_{\rm disk} {\rm PDF}(i,\Omega) d{\rm SA}}{\int_{\rm peak} {\rm PDF}(i,\Omega) d{\rm SA}} \quad (10)$$

$$\int_{\rm disk} d{\rm SA} = \int_{\rm peak} d{\rm SA}, \quad (11)$$

where SA is the solid angle measured as the contour at which the density drops to 50% of its peak value ($\sim$0.2 sr or FWHM = 15.°2). The disk membership probabilities ($1 - L_{\rm non\text{-}disk}$) are given in Table 4 and the stars' proper motion vectors are color-coded according to these probabilities in Figure 11. We note that five of the six accelerating sources are among the most likely disk members ($1 - L_{\rm non\text{-}disk} > 0.4$; see Figure 22 in Appendix E). In Lu et al. (2009), non-disk candidates were identified at the 3σ significance level ($L_{\rm non\text{-}disk} > 0.9973$), which would result in 58 stars that are not disk stars, and the remaining stars would be considered as disk members ($N_{\rm candidates} = 58$) and include all six stars with significant acceleration detections. Using this metric, the fraction of stars in our sample that are candidate disk members is 50%, which is consistent with earlier work. The true disk

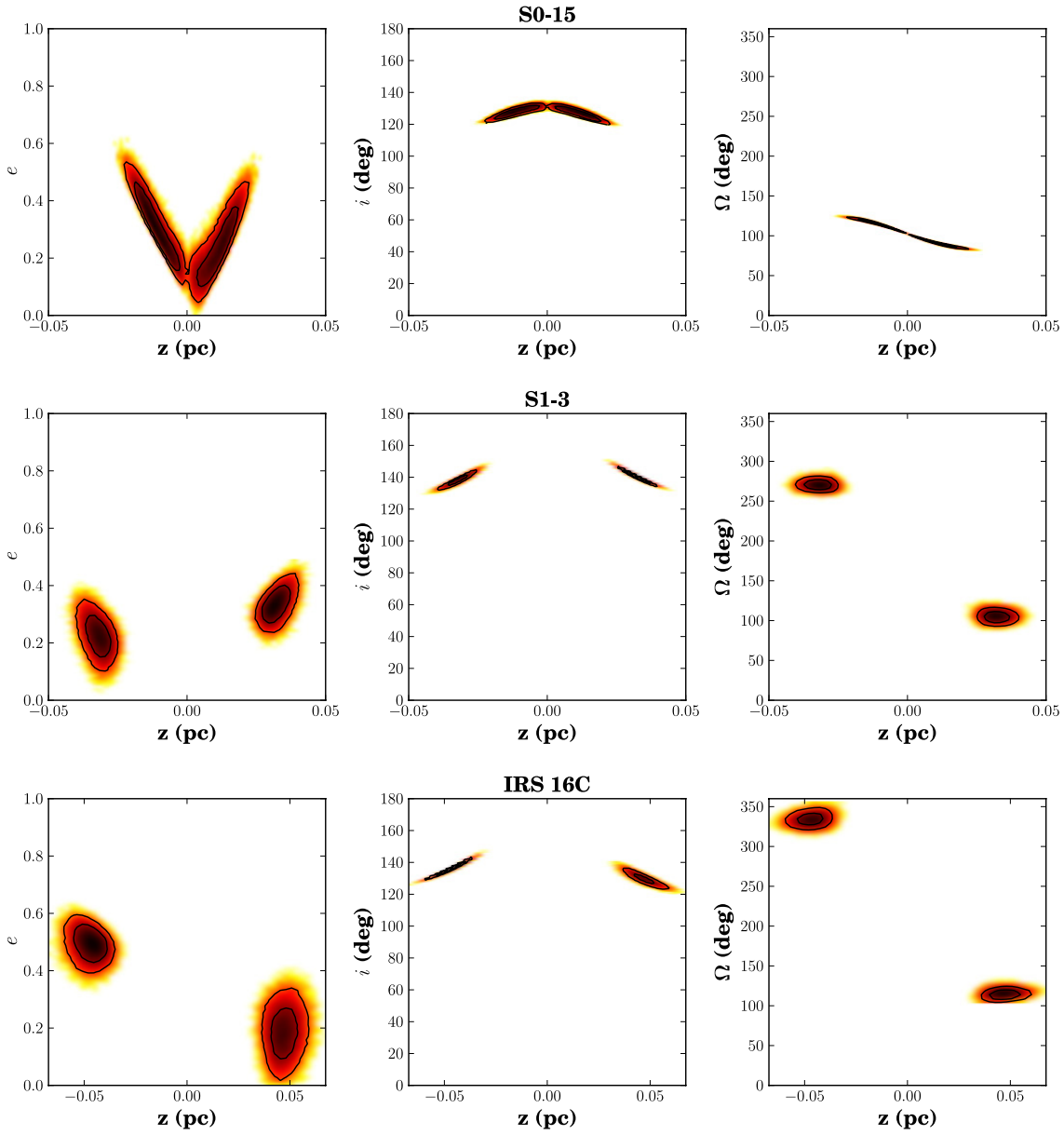

Figure 9. Probability distribution functions for eccentricity (left), inclination (middle), and angle to the ascending node (right) as a function of the line-of-sight distance for the six stars with significant accelerations in the plane of the sky. The absolute value of the line-of-sight distance, $|z|$, is precisely determined for each of these stars from their measured accelerations. The sign ambiguity of z results in the degenerate set of solutions. The stars S0-15 and S1-14 have solutions consistent with $z = 0$. The 1σ and 2σ contours of the PDFs are overplotted as solid lines.

(A color version of this figure is available in the online journal.)

fraction, however, is likely to be smaller than this and is explored below using mock data sets.

The stars in the CW disk are found to have non-circular orbits. In Figure 12, we plot the solutions of the accelerating stars separately from those of the non-accelerating stars. Only orbital solutions that fall within 15.°2 of the disk solution are included for each star, thus weighting the distribution by disk membership probabilities. Both eccentricity distributions are clearly offset from $e = 0$, with an average for the accelerating stars of $\langle e \rangle = 0.27 \pm 0.09$ and the non-accelerating stars $\langle e \rangle = 0.43 \pm 0.24$. The uncertainty on the eccentricity reported here is the standard deviation of the distribution ($\sigma_{e,\mathrm{measured}}$). Below, we explore the impact and possible bias of measurement uncertainty (since the eccentricity is a positive definite quantity) and of the uniform acceleration prior on what is observed.

The scale height of the disk (h/r) can be estimated using the velocity dispersion perpendicular to the disk plane ($\sigma_{\boldsymbol{n}}$) and the average magnitude of the 3D velocity ($\langle v \rangle$) as

$$\frac{h}{r} = \frac{\sigma_{\boldsymbol{n}}}{\langle v \rangle}, \tag{12}$$

where the velocity dispersion is corrected for the bias due to measurement uncertainties and is weighted by disk membership probability. This quantity can be related to a dispersion angle, $\Delta\theta$, about the disk plane: $h/r \sim \sqrt{1/2}\Delta\theta$ (Beloborodov et al. 2006). We find $\sigma_{\boldsymbol{n}} = 33 \pm 4$ km s^{-1} and a scale height of $h/r = 0.10 \pm 0.01$, which gives a dispersion angle of $\Delta\theta = 8.°0 \pm 1.°0$, consistent with earlier estimates (Paumard et al. 2006; Lu et al. 2009; Bartko et al. 2009). The data were also separated into two radial bins (at $R = 3.''3$) that have equal total weights (i.e., total

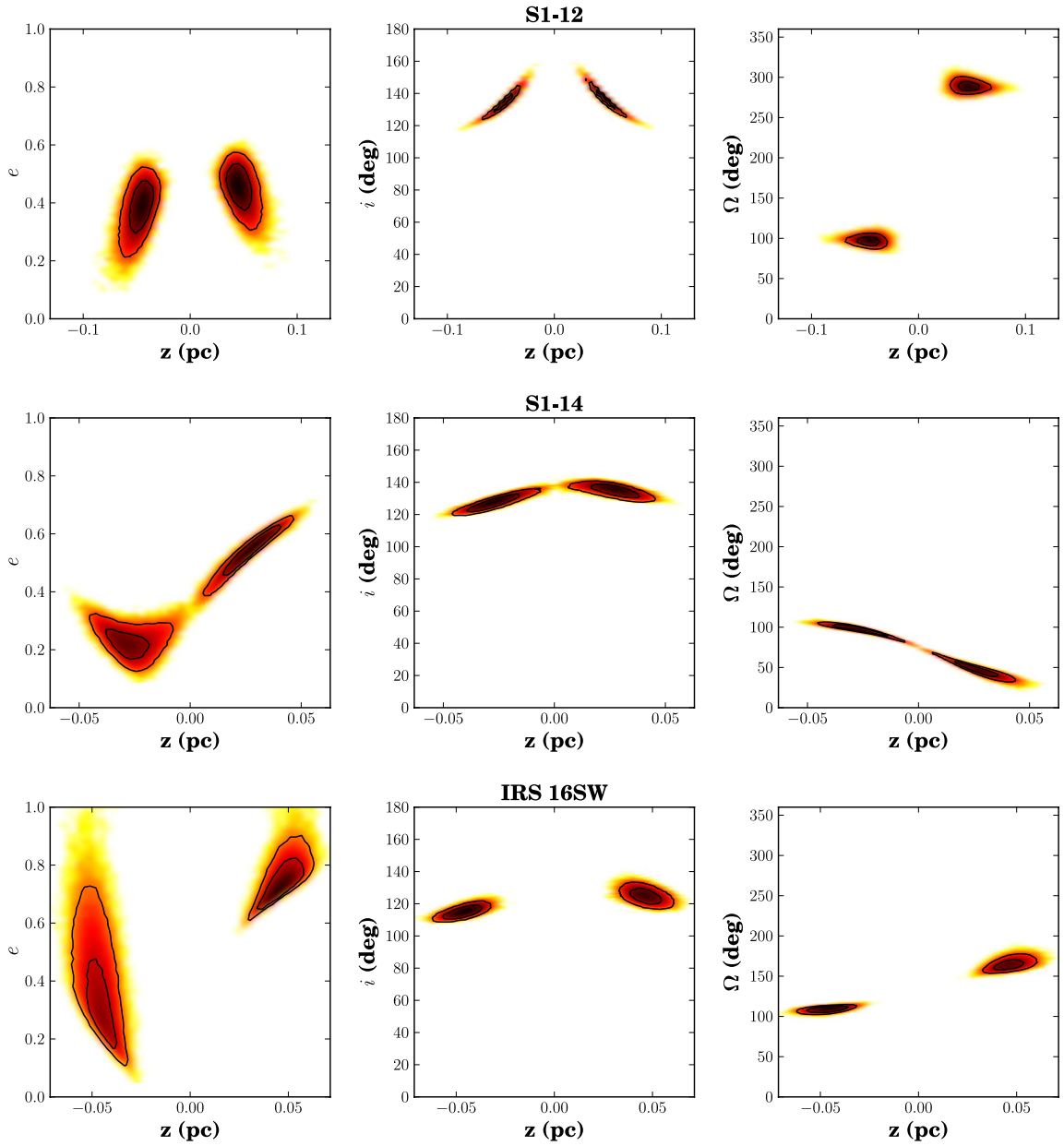

Figure 9. (Continued)

disk membership probabilities) and the scale height within each radial bin was computed. We find for the inner ($N = 42$ stars) and outer ($N = 74$ stars) bins $h/r = 0.10 \pm 0.02$ and $h/r = 0.07 \pm 0.01$, respectively. Thus, the dispersion angle of the disk does not get larger with radius.

4.2. Comparison with Simulations

4.2.1. Mock Data Sets

To explore the impacts of measurement error and the acceleration prior assumptions used in our orbital analysis, we construct mock data sets with known underlying kinematic properties. Both stars with a common orbital plane (i.e., in a stellar disk) and stars on randomly oriented orbits are modeled, allowing us to quantify our ability to reconstruct orbital elements from mock data and subsequently identify kinematic structures and their members.

In each set of simulations performed, we create mock kinematic data (x, y, v_x, v_y, v_z, a_x, a_y), add errors to each of these variables, and run our MC orbital simulations in the same way that the observed data are treated. These mock data are generated by assuming a true orbit (with elements P, e, i, Ω, ω, and T_0) around a point mass of $4.6 \times 10^6\ M_\odot$. We choose to use a point mass since including the extended mass in the analysis of the real data did not make a difference in the final results. For all stars in all simulations, T_0 is uniformly sampled from 1995 (the beginning of our observations) to 1995 + P, and ω from 0° to 360°. For stars on orbits that are randomly oriented, we sample from uniform distributions in $\cos(i)$ from 0 to 1 and in Ω from 0° to 360°. We assume the surface density profile found by Do et al. (2013) for the young stars beyond $R = 1''$, $\Sigma(R) \propto R^{-1.14}$, which when combined with the black hole mass gives the period of the orbit. The eccentricities are sampled from a thermal distribution ($n(e) \sim e$). When simulating disk stars, the semi-major axes are

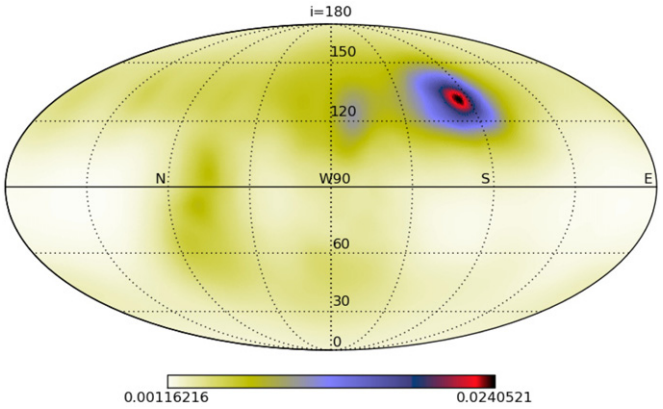

Figure 10. Density of normal vectors to the orbital planes (in stars deg^{-2}) of all 116 stars in the sample. The direction of the normal vector is described by the inclination (i; horizontal lines spaced 30° apart) and the angle to the ascending node (Ω; longitudinal lines spaced 45° apart, with the line marked E representing $\Omega = 0°$). An overdensity of 0.024 stars deg^{-2} occurs at $(i, \Omega) = (130°, 96°)$.

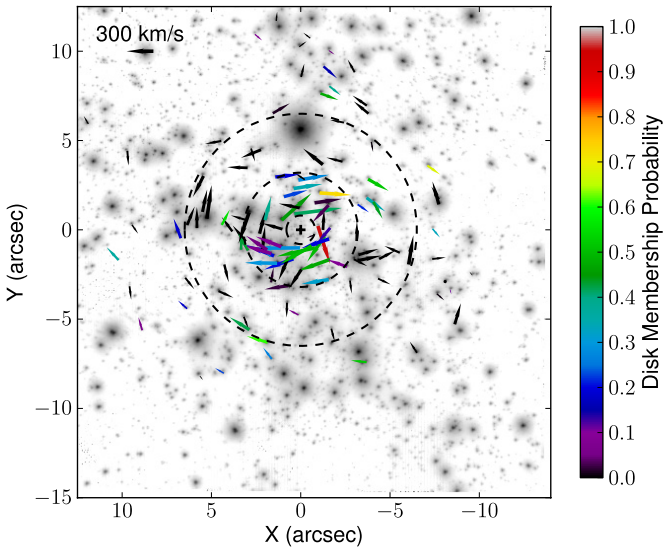

Figure 11. Velocity vectors of all 116 stars in the sample. Sgr A* is marked as a cross in the center. The arrows are color-coded according to their disk membership probability. The dashed circles mark the three radial bins discussed in Section 4.2.2 and are located at $R = 0\farcs8$, $3\farcs2$, and $6\farcs5$.

randomly sampled such that the resulting surface density profile in the disk plane follows the observed profile, $\Sigma(R) \propto R^{-1.9}$ (Paumard et al. 2006; Lu et al. 2009; Bartko et al. 2009). The orientation of the disk plane is set to that of the observed disk, $(i, \Omega) = (130°, 96°)$. The distribution of orbital eccentricities for the disk stars depends on the simulation. From these simulated orbits, we select the 3D positions, velocities, and accelerations at a particular "observation" time, which we take as 2004.2, the mean time of our actual observations. Mock accelerations are only determined for stars within $5''$ of the black hole, consistent with our treatment of the real data. We consider only those simulated stars whose projected positions are within the FOV covered by the Keck and VLT spectroscopic observations.

The noise added to the mock data is based on the observed measurement uncertainties as a function of distance from the black hole, as astrometric uncertainties tend to increase with radius (see Figure 5). We determine the minimum and maximum uncertainties in position, velocity, and acceleration of the known young stars in our sample in $1''$ radial intervals. In each trial, the uncertainties assigned to a simulated star are randomly selected from a uniform distribution between these boundaries for the appropriate radial interval (dependent on the simulated star's projected radius). We then run 10^4 MC trials in which we sample from the mock data and the assigned uncertainties for each simulated star. This results in a six-dimensional PDF representing the probability distributions for the six orbital elements. For simplicity, we only use acceleration information if the star's simulated acceleration is significant (5σ), given its assigned uncertainty. For the remaining stars, a uniform acceleration prior is used, imposing the same boundaries of the minimum acceleration allowed given a bound orbit and the maximum acceleration given the star's projected radius.

Table 5
Mock Data Sets

ID	N_{cases}	N_{stars}	$R(''')$	f_{disk}	e_{disk}
1	1000	116	0.8–14.0	0.00	···
1a	1000	40	0.8–3.2	0.00	···
1b	1000	40	3.2–6.5	0.00	···
1c	1000	40	6.5–14.0	0.00	···
2	13	100	0.8–14.0	1.00	0.00–0.5
3	110	120	0.8–14.0	0.05–0.55	0.32

Table 5 summarizes the mock data sets created and we describe their details here.

1. *Significance of kinematic structures (Section 4.2.2):* the statistical significance of a density peak in the PDF(i, Ω) map is quantified through a comparison to the density expected from a population of stars with randomly oriented orbits. To this end, we create 1000 separate data sets, each of which includes 116 stars on randomly oriented orbits (ID 1 in Table 5), and run our orbital analysis. Likewise, 1000 data sets are generated for an isotropic population of 40 stars within each of three radial bins ($0\farcs8$–$3\farcs2$, $3\farcs2$–$6\farcs5$, and $6\farcs5$–$13\farcs3$) for the purposes of quantifying the significance of substructures as a function of radius.
2. *The eccentricity distribution of disk stars (Section 4.2.3):* the eccentricity distribution of the stellar disk population is explored with mock data sets, each of which consists of a disk of 100 stars, each having the same eccentricity vector of magnitude e_0 and a direction that is randomly oriented within the disk plane, and with other orbital parameters as described above (ID 2). Thirteen data sets with the following eccentricities are modeled: $e_0 = [0.0, 0.05, 0.1, 0.15, 0.2, 0.25, 0.27, 0.3, 0.32, 0.35, 0.4, 0.45, 0.5]$. These data sets are run through our orbital analysis and the resulting eccentricity distributions are compared to that of the observed distributions in order to determine the eccentricity to be used for simulations of disk stars. The models with $e_0 \sim 0.3$ give the most similar eccentricity distributions (in a least-squares sense; see Section 4.2.3), and we therefore choose to use $e_0 = 0.3$ for modeling disk stars (see next item).
3. *Fraction of stars in disk (Section 4.2.4):* orbits of both disk stars and stars with isotropically distributed orbital planes are generated to estimate the true disk fraction (ID 3). Eleven disk fractions are tested, from $f_{disk} = 5\%$ to $f_{disk} = 55\%$, spaced every 5% and for a total of 120 stars. For each disk fraction, 10 independent mock data sets are generated, resulting in 110 sets in total. The disk stars' orbital properties are $i = 130°$, $\Omega = 96°$, and $e = 0.32$. The

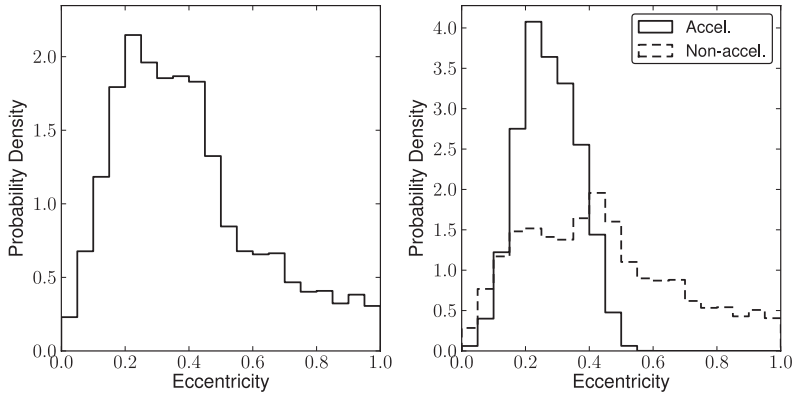

Figure 12. Left: eccentricity distribution of the clockwise disk. All orbital solutions falling within 15.°2 of the disk are included, thereby weighting the distributions by disk membership probability. Right: eccentricity distributions shown separately for likely disk members with acceleration detections (solid) and without (dashed).

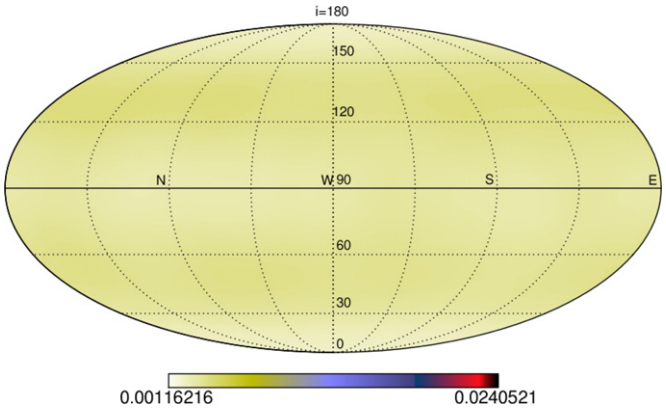

Figure 13. Average PDF(i, Ω) map in units of stars deg^{-2} for an isotropic population of 116 stars. The distribution of normal vectors is relatively uniform over the sky, with a slight deficit of edge-on orbits ($i = 90°$) due to the uniform acceleration prior.

eccentricity was chosen based on the orbit simulations on the mock data above (ID 2).[10]

4.2.2. Significant Kinematic Features

To quantify the significance of the peaks in the observed PDF(i, Ω) map, the peak density is compared to the density of normal vectors expected for an isotropic population. Density maps were produced for all 1000 simulated data sets (ID 1 in Table 5). Figure 13 shows the average PDF(i, Ω) map for the isotropic data. The normal vectors are nearly uniformly distributed over the sky with a slight deficit of edge-on orbits ($i = 90°$) due to the uniform acceleration prior. This prior results in smaller line-of-sight distances on average than the simulated stars' true distances, and small $|z|$ will favor face-on orbits over edge-on orbits. Due to this slight dependence on inclination, we split the maps up into inclination bins spaced every 20° from 0° to 180° and determine the peak density within each bin. The average, $\rho_{\mathrm{iso},i}$, and standard deviation, $\sigma_{\mathrm{iso},i}$, of the peak densities over all 1000 simulations are then calculated for each inclination bin, i. We then quantify the significance of any density enhancements, ρ_{peak}, in our data as

$$S = \frac{\rho_{\mathrm{peak}} - \rho_{\mathrm{iso},i}}{\sigma_{\mathrm{iso},i}}, \quad (13)$$

where the inclination bin, i, is selected based on the location of the observed peak density.

An isotropically distributed set of stars has an average peak density of $\rho_{\mathrm{iso},i} = 0.006 \pm 0.001$ stars deg^{-2}. The peak density of the observed normal vectors for the entire sample is $\rho_{\mathrm{peak}} = 0.024$ stars deg^{-2}, and has a significance of $S = 20.7$.

The global structure of the disk can be described by studying its orientation as a function of radius. To this end, we group stars into three radial bins, selecting radial intervals such that roughly equal numbers of stars (∼40) fall in each bin, similarly to the method of Bartko et al. (2009). The radial intervals used are 0.″8–3.″2, 3.″2–6.″5, and 6.″5–13.″3.[11] Figure 14 shows the resulting PDF(i, Ω) for each bin. The significance of a density enhancement found in either of these maps is determined as in Equation (13), but relative to 40 isotropically distributed orbits within the radial bin of interest.

The peak density of normal vectors in the inner radial bin ($N = 39$ stars) is 0.014 stars deg^{-2} and is found at (i, Ω) = (129°, 98°), consistent with the angles found when using the entire sample. The significance of this feature is $S = 20.3$ and is the only structure detected at these radii. The middle radial bin ($N = 38$) shows no significant peak ($S_{\mathrm{max}} = 1.4$), which differs from what was found by Bartko et al. (2009). Finally, the outermost bin ($N = 39$) shows an overdensity of 0.004 stars deg^{-2} near (i, Ω) = (117°, 192°), consistent with the feature seen at large radii by Bartko et al. (2009), and has a marginal[12] significance of $S = 5.1$. We caution, however, that this feature is a result of mainly three stars and that the outer radial bin is not sampled uniformly in azimuth. While Bartko et al. (2009) report a significant CW feature in each of their three radial bins at different angles, hence leading to the claim of a warp, we do not detect any features at intermediate radii. Furthermore, the previously proposed counterclockwise disk is not detected in any radial bin in this work. We therefore conclude that the population not on the CW disk (aside from the three stars with

[10] An earlier analysis of the observations revealed that a disk with $e = 0.32$ produced the most similar eccentricity distributions. The updated value of $e = 0.3$ does not significantly affect the results.

[11] The edges of the three radial bins we use are slightly different than those used by Bartko et al. (2009) since the two studies contain different sample sizes and the radial bins were defined such that they each contained an equal number of stars. In our work, we define the edges of the bins using $R = 0.''8$, $3.''2$, and $6.''5$ and include ∼40 stars per bin, whereas Bartko et al. (2009) use $R = 0.''8$, $3.''5$, and $7''$ and had ∼30 stars per bin. This does not affect the overall conclusions.

[12] Based on the isotropic simulations of stars in the outer radial bin, the distribution of peak densities is slightly skewed, with peak densities of 0.004 stars deg^{-2} or greater occurring once out of the 700 total simulations run for this radial bin. Thus, $S = 5.1$ corresponds to 99.86%, which for a Gaussian distribution is $\sim 3.1\sigma$. One must therefore be cautious when interpreting features detected at such levels.

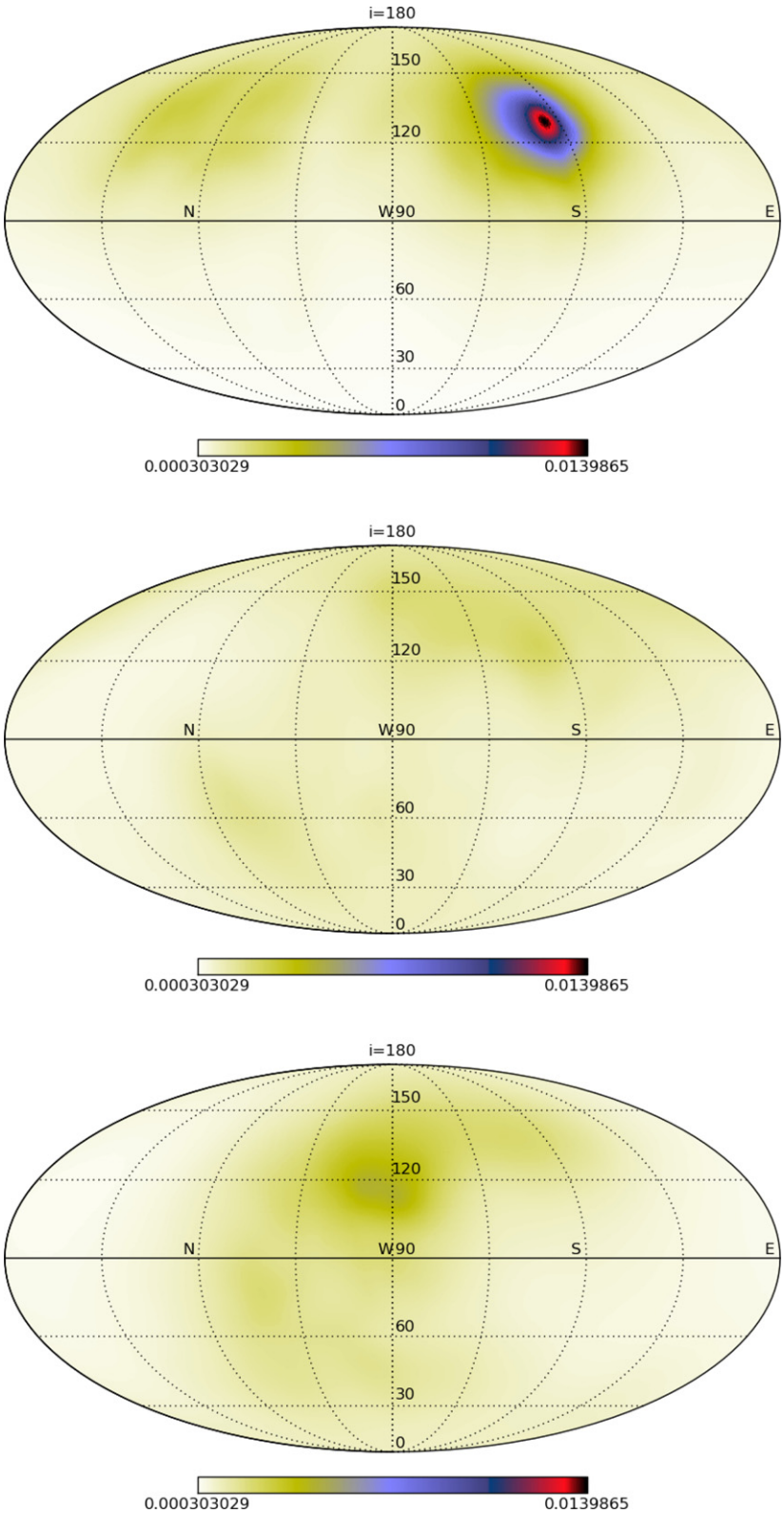

Figure 14. Density of normal vectors for stars in the three separate radial bins: 0.″8–3.″2 (top), 3.″2–6.″5 (middle), and 6.″5–13.″3 (bottom). The clockwise disk feature at $(i, \Omega) = (130^\circ, 96^\circ)$ is prominent in the inner radial bin and shows a decrease in density with radius. The degenerate orbital solutions associated with the CW disk stars are seen as the slight density enhancement near $(i, \Omega) \sim (130^\circ, 300^\circ)$ in the top panel. The middle radial interval shows hints of the CW disk and extended structure around this location. In the outermost radial bin, a density enhancement is seen at $(i, \Omega) = (117^\circ, 192^\circ)$. The same scaling is used in each plot to show the relative strength of the features. Recall that the horizontal lines represent i and are spaced 30° apart and the longitudinal lines represent Ω and are spaced 45° apart, with the line marked E representing $\Omega = 0^\circ$.

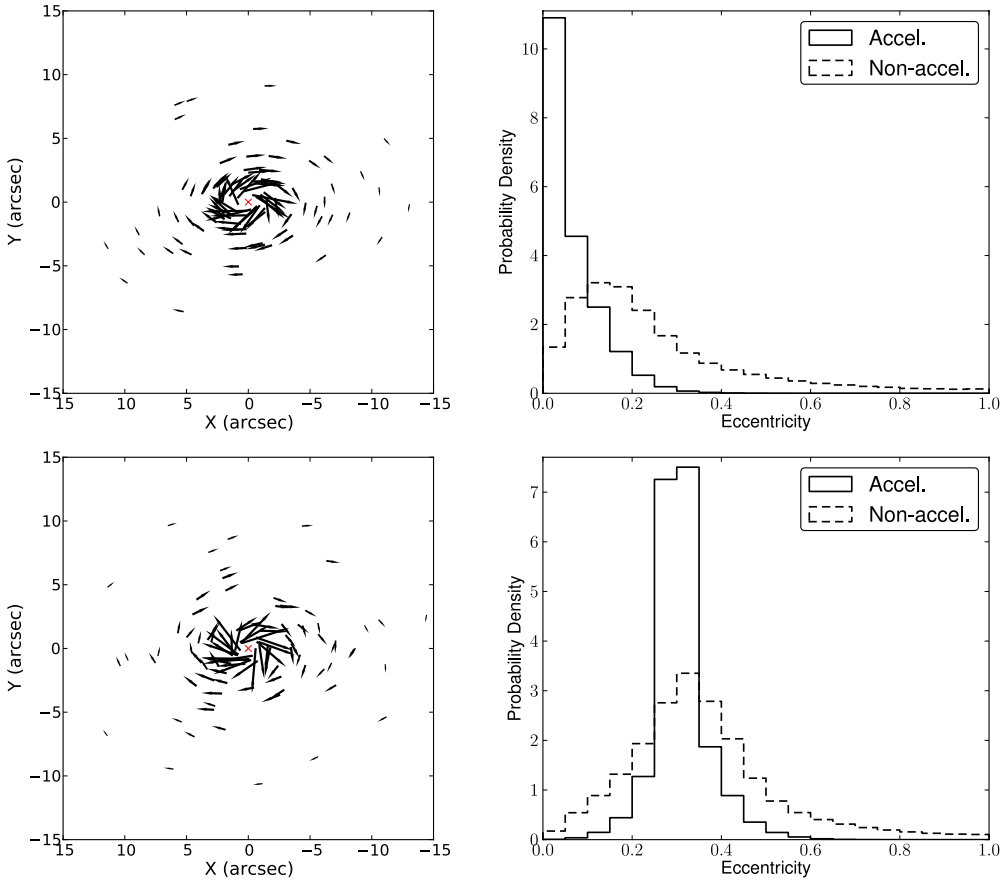

Figure 15. Simulated circular (top) and eccentric ($e = 0.3$; bottom) orbits each consisting of 100 stars within a disk with an orbital plane orientation similar to that of the observed disk. For each simulation, the generated velocity vectors of the stars are shown on the left, with the location of the black hole being marked as a red X at the center. The eccentricity distributions of the accelerating (solid) and non-accelerating (dashed) stars from each simulation are shown on the right. The orbits of the accelerating stars are more accurately determined, as expected. Based on these simulations, the observed eccentricity distribution in Figure 12 cannot be a result of measurement bias added to an intrinsically circular disk.

(A color version of this figure is available in the online journal.)

common orbital planes in the outer radial bin) is consistent with an isotropic distribution within the measured uncertainties.

4.2.3. Eccentricity Distribution of Candidate Disk Stars

The resulting eccentricity distributions from the orbital analysis on the simulated disks with a range of input eccentricities (ID 2; see Figure 15 for two cases) were compared to the observed values. The χ^2 statistic was calculated separately for the eccentricity distributions of accelerating and non-accelerating stars (Figure 16). The true eccentricity value at which χ^2 is minimized based on a Gaussian fit to the data is $e_0 = 0.27$ for the accelerating stars and $e_0 = 0.23$ for the non-accelerating stars. We therefore conclude that the young stars in the disk have a true eccentricity of $e = 0.27$.

Measurement uncertainties of the individual eccentricities can both bias the observed average values and increase the width of the eccentricity distribution. For the simulated case of $e_0 = 0.3$ with no intrinsic width, the observed average and rms values are 0.31 ± 0.06 and 0.42 ± 0.21 for the accelerating and non-accelerating stars, respectively. This shows that there is a bias in the average eccentricity that is more substantial for the non-accelerating stars. Furthermore, if we treat the rms values from the simulation as a bias term and subtract in quadrature from the observed rms values, then it appears that most of the spread in the observed eccentricities can be accounted for by measurement uncertainties. We obtain a formal estimate of the intrinsic rms of 0.07 and 0.12 for the accelerating and non-accelerating stars, respectively.

Based on these simulations, our final eccentricity estimate for the young stars is $\langle e \rangle = 0.27 \pm 0.07$. This is the first time the measurement bias has been quantified via simulations and explicitly accounted for in estimates of the eccentricities of stars on the CW disk. The eccentricities are slightly lower than previously determined (Beloborodov et al. 2006; Lu et al. 2009; Bartko et al. 2009), which in part is because of the removal of measurement bias in this work and the more precise eccentricity measurements of the accelerating stars.

4.2.4. True Disk Fraction

Our ability to estimate the true fraction of disk members can be quantified using the orbital analysis of mock data involving a combination of disk and isotropic stars (ID 3 in Table 5). For each disk fraction simulation, a density map of (i, Ω) is generated and compared to that of the observed data. We compute the squared difference in density between the model and the observations at each pixel, j, in the (i, Ω) map that is within 30° from the location of the observed peak, and sum over all pixels ($N_{\rm pix} = 3292$). We refer to this quantity as ξ:

$$\xi = \sum_{j}^{N_{\rm pix}} (\rho_{{\rm model},j} - \rho_{{\rm observed},j})^2. \quad (14)$$

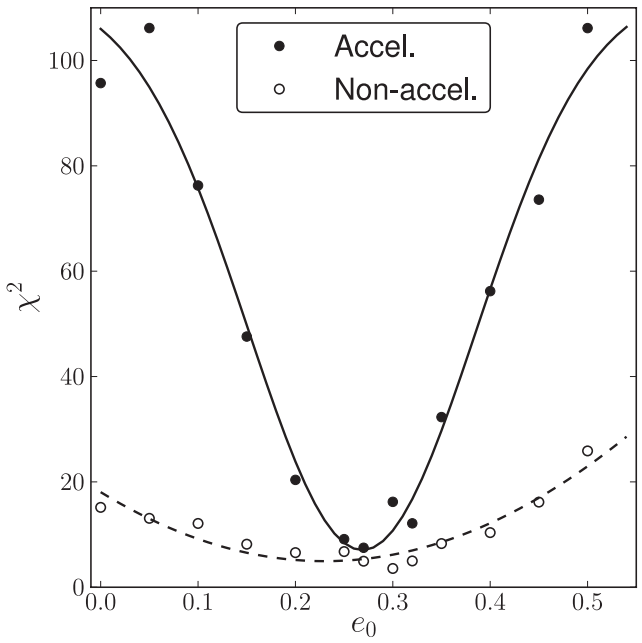

Figure 16. χ^2 as a function of initial eccentricity of simulated disk stars. For each e_0 tested, χ^2 was calculated by comparing the resulting normalized eccentricity distribution to that of the observed candidate disk stars separately for the accelerating (filled points) and non-accelerating (unfilled points) stars (we assume all errors are unity). Based on a Gaussian fit to these data, χ^2 is minimized at $e_0 = 0.27$ for accelerating (solid curve) and $e_0 = 0.23$ for non-accelerating (dashed curve) stars.

The left panel of Figure 17 shows these results, averaged over the 10 trials for each disk fraction, with a second-degree polynomial fit to the data. Based on this fit to the data, the disk fraction for which ξ is minimized is $f_{\rm disk} = 0.21 \pm 0.02$, where the uncertainty is taken as the rms error on the minimum ξ obtained from fits on each of the 10 trials. The method for identifying disk stars, described in Section 4.1, can also be tested using these disk fraction simulations. The right panel of Figure 17 shows the ratio of the estimated number of candidates from this method to the true number of disk members for each model, which reveals the degree of contamination from the non-members. After fitting a functional form to these data, we find that the number of disk members is overestimated by a factor of ∼2.4 for $f_{\rm disk} = 0.21$. Thus, in the observed data, the number of candidates ($N_{\rm candidates} = 58$) is an overestimate, and we take the true number of disk members to be $58/2.4 \sim 24$. We note that 24 is ∼21% of our sample, which validates our finding of a disk fraction of 21%. For the 10 cases that were run using $f_{\rm disk} = 0.20$, the combined histogram of disk membership probabilities is shown in Figure 18. With the conservative cut used to select candidate disk members described in Section 4.1, all true disk members are identified but we also see an abundance of contaminants from the isotropic population.

From these simulations, we also find that that there is a small dependence of the disk membership probability on the P.A. from the disk's line of nodes for stars with no acceleration information (see Appendix E), whose orbital solutions are more sensitive to the prior for the line-of-sight distance (Section 3.3). If the disk membership probability is to be used for identifying specific disk candidates in the observed sample, the stars' P.A.s must also be considered. The most likely 24 true disk members are listed in Table 9 of Appendix E.

5. DISCUSSION

We have performed a detailed kinematic analysis on the central parsec young star population using high precision astrometry over a longer time baseline than in any other such study. Combined with RV measurements, we have confirmed the existence of the CW stellar disk and have shown there is no significant counterclockwise structure, in agreement with Lu et al. (2009). Through a series of orbital analyses on mock data sets, we showed that 20% of the stars in our sample are true members of the disk, a factor of more than two lower than previous estimates, which were based on disk candidacy alone (Lu et al. 2009; Bartko et al. 2009). The intrinsic average eccentricity of disk members is $e = 0.27$, and we find no significant detection of the disk beyond 3.″2. Here we discuss the implications of these findings and explore the relationship between the B stars and O/WR stars in our sample.

5.1. Disk Remnant

Our orbital analysis of mock data sets reveals that the disk is made up of 20% of the sample. Thus, assuming a single-disk origin, we are likely observing the remnants of what used to be a more densely populated disk. For such a scenario, some dynamical mechanism(s) that can excite the orbits such that 80% of the stars are no longer kinematically associated with the original disk must be invoked. It was shown that two-body relaxation is not sufficient to explain the high inclinations relative to the CW disk (e.g., Cuadra et al. 2008). Vector resonant relaxation with the surrounding stellar cluster, on the other hand, can lead to a strongly warped disk (Kocsis & Tremaine 2011). It is unclear, however, whether this mechanism can explain the observed properties of the stars both on and off the disk. Massive perturbers, such as an IMBH can lead to strong scattering off the disk (Yu et al. 2007). One of the major challenges to this scenario, however, is the lack of evidence for an IMBH at the GC. One massive perturber that is observed, however, is the circumnuclear disk (CND) located at $R \sim 1.5$ pc (CND; Christopher et al. 2005). Šubr et al. (2009) first investigated the influence of the CND on a thin stellar disk and found that differential precession can lead to a configuration that is similar to what is observed. The effects of the CND will be most pronounced at the outermost portions of the stellar disk, erasing any observable disk-like structure at large radii while leaving the innermost orbits untouched (Šubr et al. 2009; Haas et al. 2011a, 2011b). This is qualitatively consistent with the observations reported here.

Figure 19 shows the *K*-band luminosity function (KLF) of the sample, plotted separately for the most likely disk members ($N = 28$) and non-members ($N = 88$; see Appendix E). A two-sample KS test yields a probability of 87% that the distributions are the same, lending support to a common origin scenario (although not necessarily a common disk origin). It is still unclear whether all of the stars formed in a single disk. Indeed, the existence of a second, less massive disk with counterclockwise orbiting stars has remained controversial (Genzel et al. 2003; Paumard et al. 2006; Bartko et al. 2009; Lu et al. 2009) and is not supported by the observations reported here. However, if two highly inclined disks of different masses existed at one point in the GC, their mutual interaction would lead to the ultimate destruction of the lower mass disk within 5 Myr and we would therefore not observe the structure today (Löckmann & Baumgardt 2009). While this may explain the lack of counterclockwise structures

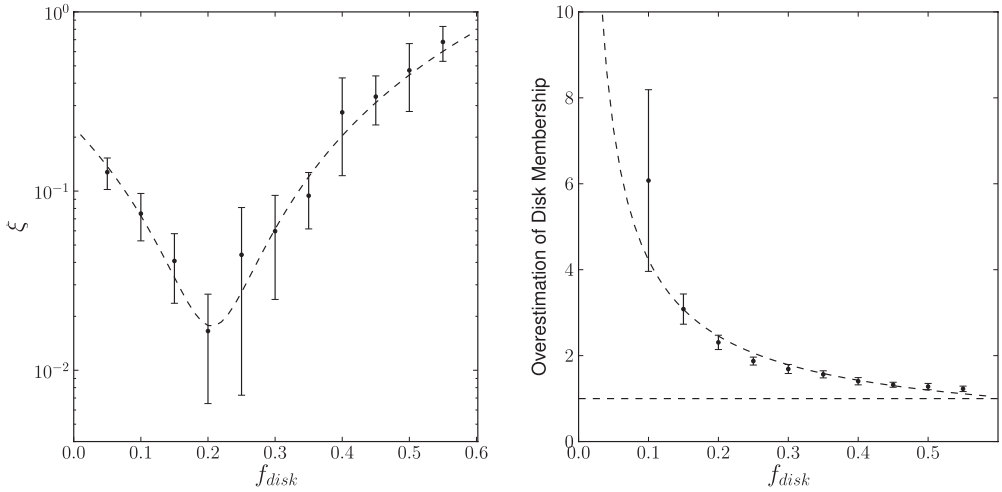

Figure 17. Left: sum of the squared differences in density between the disk fraction models and the observations (see Section 4.2.4), averaged over the ten independent trials run for each disk fraction model. A second-order polynomial was fit to the data (dashed curve) and gives a minimum ξ value at $f_{\rm disk} = 0.21$, implying a true disk fraction in our sample of 21%, or ∼24 stars. Right: the level to which the true number of disk members is overestimated in each disk-fraction model, again averaged over the 10 trials run for each disk fraction model. As a visual reference, a dashed line marks where the number of candidate disk stars equals the true number in each simulation. Note that the *Y*-axis is truncated for clarity. For $f_{\rm disk} = 0.21$, the number of disk candidates is overestimated by a factor of 2.4.

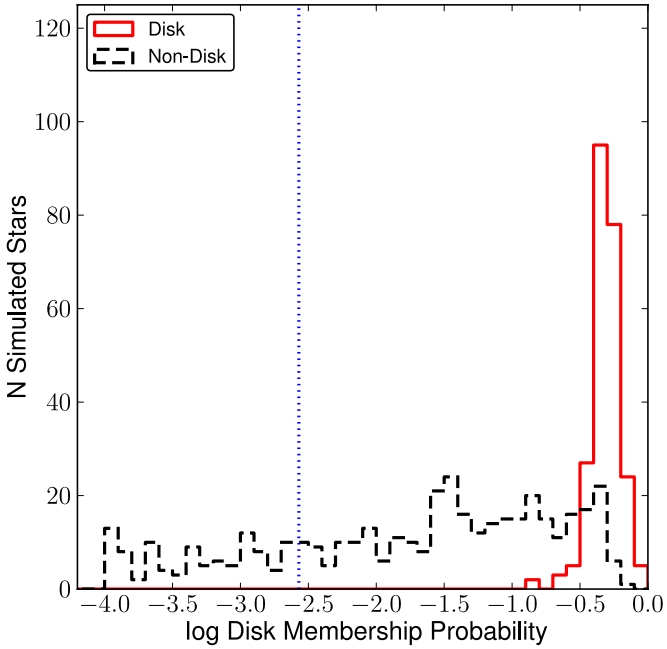

Figure 18. Combined histogram of disk membership probabilities $(1-L_{\rm non\text{-}disk})$ for the 10 simulations with $f_{\rm disk} = 0.2$. True disk members are shown as the red solid histogram, while the isotropic population is shown as the black dashed histogram. The vertical blue dotted line marks the criteria used for selecting candidate disk members, namely $(1 - L_{\rm non\text{-}disk}) > 0.0027$. While this conservative threshold identifies all true disk members as candidates, there is an abundance of contaminants, even at the highest probabilities. An additional 544 isotropic stars were cut off to the left of the figure for clarity.

(A color version of this figure is available in the online journal.)

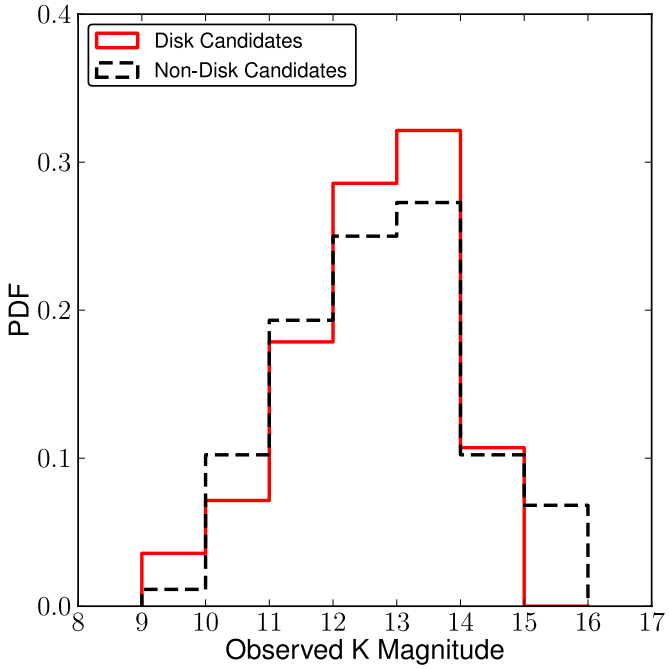

Figure 19. Normalized distribution of *K*-band luminosities of the most likely members (see Appendix E) of the disk (red solid) and the remaining stars (black dashed). A two-sample KS test yields a probability of 87% that the most likely disk members have the same KLF as the remainder of the sample. We caution that the *K*-band magnitudes in this figure are observed magnitudes and have not been corrected for completeness or extinction effects.

(A color version of this figure is available in the online journal.)

in our analysis, such a scenario would demand that two star formation events at or near the GC occurred within 2 Myr of one another.

5.2. Eccentricity of Disk Stars

The orbits of the disk members are found to be eccentric, with a distribution that peaks near $e = 0.3$. We show above that these results cannot be explained by a circular disk ($e = 0$) whose eccentricity is biased upward due to measurement error. Furthermore, the fact that five of the six stars with reliable acceleration measurements are likely disk members and collectively have an eccentricity of $\langle e \rangle = 0.27 \pm 0.07$ gives us confidence that the disk is eccentric. We also find that the distribution is unimodal, lacking the high eccentricity bin ($e > 0.9$) reported by Bartko et al. (2009), which those authors claim may have been a result of contamination by non-disk members.

The observed eccentricities can be used to constrain formation scenarios for the disk. Levin et al. (2005) showed that the

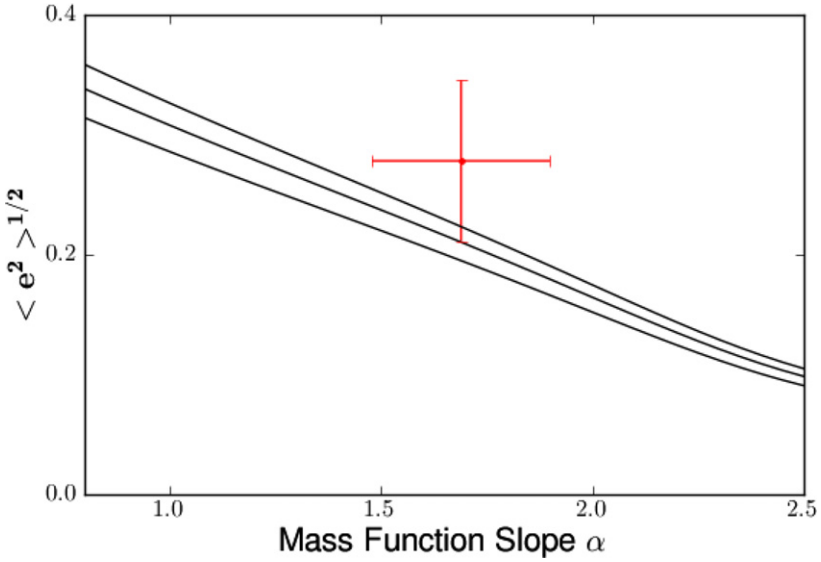

Figure 20. Predicted rms eccentricity (black curves) of 50 stars, each with mass $M = 25\ M_{\odot}$, resulting from two-body interactions within a stellar disk with various mass function slopes. This is a version of Figure 4 in Alexander et al. (2007), which has been updated to reflect the latest black hole mass estimates ($4 \times 10^6\ M_{\odot}$) and a recent estimate of the age of the young star population from Lu et al. (2013) of 3.65 ± 0.87 Myr. From bottom to top, the three curves represent the rms eccentricity after 2.78 Myr, 3.65 Myr, and 4.52 Myr, respectively. The red point shows the rms eccentricity and estimated uncertainty of our best measured stars ($\langle e^2 \rangle^{1/2} = 0.28 \pm 0.07$) and the latest estimate of the mass function slope ($\alpha = 1.7 \pm 0.2$) from Lu et al. (2013). The observed values are within 1σ of the predicted values from the Alexander et al. model.

(A color version of this figure is available in the online journal.)

circular inspiral of a cluster anchored by an IMBH can produce significant eccentricities for some of the cluster stars. Similarly, Berukoff & Hansen (2006) found that the stars' eccentricities will mirror the eccentricity of the cluster's IMBH with a scatter of roughly ±0.1–0.2. While these values are somewhat consistent with what we find for disk members in this work, we caution that the cluster-infall scenario suffers from many theoretical and observational challenges, as discussed in Section 1.

Several in situ formation scenarios in which the stars form in either an initially circular or eccentric gaseous disk have been proposed in attempts to explain the previous estimations of the eccentricity distributions and kinematic structures (Nayakshin et al. 2007; Alexander et al. 2008; Bonnell & Rice 2008; Mapelli et al. 2008; Yusef-Zadeh & Wardle 2008; Wardle & Yusef-Zadeh 2008; Hobbs & Nayakshin 2009; Mapelli et al. 2012). In all of these scenarios, it is necessary to include interactions within the disk (Alexander et al. 2007; Kocsis & Tremaine 2011) and any surrounding cusp (Madigan et al. 2009; Löckmann & Baumgardt 2009; Löckmann et al. 2009) over the lifetime of the stars to produce an eccentricity distribution that can be compared with present-day values. However, the viability of these scenarios and the need for more extreme scenarios that invoke initially eccentric disks must be re-examined in light of our revised understanding of, for example, the young stars' eccentricity distribution (this study), their mass function and age (Lu et al. 2013), and the stellar cusp (Do et al. 2009; Buchholz et al. 2009; Bartko et al. 2010; Do et al. 2013). In particular, the apparent lack of a stellar cusp and the lower eccentricity distribution of the stars in the disk simplify the dynamics. Thus, we revisit a simpler origin scenario in which stars form in a circular gaseous disk and examine the effects of two-body interactions on the stellar orbits (Alexander et al. 2007). The degree to which the eccentricities are excited depends on both the age and the mass function of the population. Using the latest values of the mass function slope of $\alpha \sim 1.7$ and age of ∼3.9 Myr (Lu et al. 2013), we estimate the expected rms eccentricity after dynamical evolution of the stars (Figure 20; R. Alexander 2012, private communication). This is a version of Figure 4 of Alexander et al. (2007),[13] where here we show the final eccentricities expected after 2.78 Myr, 3.65 Myr, and 4.52 Myr, which spans the $\sim 1\sigma$ range of the Lu et al. estimates for the age of the population.[14] For the latest age and mass function slope of the young stars, the expected rms eccentricity agrees with our observed value to within 1σ. We conclude that our results are consistent with formation in a circular gas disk, which has been proposed by others (Nayakshin & Cuadra 2005; Alexander et al. 2007; Löckmann & Baumgardt 2009) and which does not require radially infalling gas clouds or a stellar cusp.

5.3. Disk Structure

Our analysis of the radial structure of the disk reveals a prominent CW disk between $r = 0\farcs8$ and $3\farcs2$ and no other significant features until $r > 6\farcs5$, where a set of three co-orbiting stars is evidenced. These two CW structures are offset from one another by ∼77°, with the outer feature being much less significant than the feature seen at small radii. Due to the lack of structure at intermediate radii, we do not find evidence of a warped disk, as found by Bartko et al. (2009).[15] Our data support the existence of a single CW disk with a radial extent of at least $r \sim 3\farcs2$. The feature seen at large radii may be a small cluster or a filamentary structure such as those found in simulations of cloud–cloud collisions (Hobbs & Nayakshin 2009) and of single-cloud infall (Lucas et al. 2013), although the stellar masses ($<2\ M_{\odot}$) in those simulations were much

[13] Alexander et al. (2007) use Γ to denote the mass function slope, where $\Gamma = 2.35$ is the Salpeter slope. However, Γ generally represents the logarithmic slope (1.35 for Salpeter), and α is typically used to denote the linear slope (see e.g., Bastian et al. 2010).

[14] The ages used in Figure 20 are from an early version of Lu et al. (2013), but are within 1σ of their published age estimate for the young stars.

[15] In Table 3 of Bartko et al. (2009), there is a mistake in the i and Ω angles reported for their outer radial bin. While their reported angles ϕ and θ are consistent with the corresponding plot in their Figure 11, the conversion to i and Ω in Table 3 is incorrect. The correct values are $(i, \Omega) = (118°, 179°)$.

lower than what is observed. We caution, however, that more uniform sampling of the outer radial bin is necessary to make a definitive claim about any kinematic structures.

5.4. The Relation of the B Stars to the Disk

The original claim of a stellar disk in the GC was based on a kinematic analysis that included only O and WR stars, as these were the only known young stars at the time (Levin & Beloborodov 2003). It is unclear how the more recently identified B-type main sequence stars (Allen et al. 1990; Krabbe et al. 1991, 1995; Blum et al. 1995; Tamblyn et al. 1996; Najarro et al. 1997; Ghez et al. 2003; Paumard et al. 2006; Bartko et al. 2010; Do et al. 2013) are associated with the O/WR population, if at all. While the age of the O/WR stars is estimated at ∼3–8 Myr (Paumard et al. 2006; Lu et al. 2013), the B stars have main sequence lifetimes of up to ∼30 Myr for the faintest stars in our sample ($K = 15.9$) and therefore may not have originated in the most recent star formation event. However, recent statistical analysis of the B stars' h-statistic, $h = (x v_y - y v_x)/\sqrt{G M_{\rm BH} R}$, suggests that brighter B stars ($K =$ 14–15) may be more consistent with formation in a disk than by binary star infall (Madigan et al. 2013). Our analysis provides a more direct disk-association test with the use of acceleration measurements or constraints and RV information.

If the B stars are, in fact, unrelated to the disk stars, then their inclusion in the analysis of Section 4.2.4 would decrease the significance of any kinematic features and lead to an artificially low disk fraction. After excluding B stars having $K > 14$ ($N =$ 18 stars), we repeat our analysis and simulations for the O/WR stars ($N = 98$ stars). The resulting analysis gives a location of the peak density at $(i, \Omega) = (130^\circ, 96^\circ)$, which is identical to that found with the full sample with a slightly reduced significance ($S = 13.3$ compared to $S = 20.7$ for the full sample). The O/WR sample was also divided into the inner, middle, and outer radial bins ($N = 29$, 35, and 34 stars, respectively), and we repeated the analyses looking for significant kinematic features. In the inner bin, we find a strong peak at $(i, \Omega) = (124^\circ, 103^\circ)$, with $S = 17.9$. Again, there is no significant feature in the middle bin ($S_{\rm max} = 1.1$). Finally, the outer radial bin shows a peak at $(i, \Omega) = (117^\circ, 192^\circ)$ with $S = 6.0$, slightly more significant than the results from the full sample. We therefore conclude that the overall kinematic structure remains the same whether B stars are included in our analysis or not.

We tested the effects of the B stars on the disk fraction by repeating the disk fraction simulations using 98 stars and comparing the results to the density map of the observed O/WR sample. The value of ξ (Equation (14)) is minimized at $f_{\rm disk} =$ 0.20 as compared to $f_{\rm disk} = 0.21$ for the full sample. The similarity in these values with those from our original analysis leads us to conclude that the inclusion of the B stars does not impact the true disk fraction.

Finally, we created a PDF(i, Ω) density map for just the 18 B stars in our sample (Figure 21). Given the decrease in the number of stars, the density at each pixel in the sky was calculated using the nearest 4 neighbors (approximately 20% of 18). The peak density (0.002 stars deg^{-2}) is found at $(i, \Omega) =$ $(136^\circ, 85^\circ) \pm (6^\circ, 12^\circ)$, which is within 1σ of the peak location using the full sample. The significance of this feature is $S =$ 6.0 as compared to the expected density of normal vectors for an isotropic population of 18 stars. Repeating the disk fraction simulations, but with a total of 18 stars, we find a minimum ξ value at $f_{\rm disk} = 0.23$, which is consistent with the results from the full sample in which 20% of the B stars were identified as disk members (Table 9). These stars are S1-8 ($K = 14.1$), S3-190 ($K = 14.0$), and S10-32 ($K = 14.4$). This suggests that the disk fraction does not change with magnitude and therefore that the B stars on the disk formed in the same starburst as the O/WR stars. Furthermore, given the similarity in the observed KLFs of the disk and non-disk members (Figure 19), most of the brightest B stars ($K < 15$) whose main sequence lifetimes are $t < 13$ Myr, likely formed with the O/WR stars. The results from the analyses done on each subset of our sample are shown in Table 6.

Table 6
Disk Properties by Sample

K	$N_{\rm stars}$	$(i, \Omega) \pm (\sigma_i, \sigma_\Omega)$[a]	S	$f_{\rm disk}$
All	116	$(130^\circ, 96^\circ) \pm (2^\circ, 3^\circ)$	20.7	0.21 ± 0.02
<14	98	$(130^\circ, 96^\circ) \pm (2^\circ, 2^\circ)$	13.3	0.20 ± 0.02
$\geqslant 14$	18	$(136^\circ, 85^\circ) \pm (6^\circ, 12^\circ)$	6.0	0.23 ± 0.11

Note. [a] Uncertainties in the peak location are estimated as the rms error from the $f_{\rm disk} = 0.2$ disk fraction simulations done for each sub-sample.

6. CONCLUSIONS

We have analyzed the orbits of 116 young stars in the GC between projected radii $R = 0\farcs8$–$13''$ (∼0.032 pc–0.52 pc). Our acceleration uncertainties are, on average, 10 μas yr^{-2} and are a factor of six smaller than in our previous efforts (Lu et al. 2009). We have thus been able to make six significant acceleration measurements outside the central arcsecond ($R = 1''$) and out to $R = 1\farcs5$ (∼0.06 pc), which provides the stars' line-of-sight distances and enables precise orbital parameter estimates. We confirm with marginal significance the existence of the CW disk, which has an orbital plane oriented at $(i, \Omega) = (130^\circ, 96^\circ)$. With simulations of mock data sets of disk stars and an isotropically distributed population, we have shown that the true disk fraction of young stars is ∼20%, a factor of ∼2.5 lower than previous estimates, suggesting that we are currently observing a remnant disk. The kinematic properties of the brightest B stars are similar to those of the O/WR stars, suggesting a common star formation event. The opening angle of the disk is ∼8° and our data do not reveal a change in the direction of the orbital plane as a function of radius. The mean eccentricity of the members of the CW disk is $\langle e \rangle = 0.27 \pm 0.07$. Given the recent finding by Lu et al. (2013) regarding the initial mass function and the age of the population, which is consistent with earlier work by Paumard et al. (2006), the eccentricities of the disk stars can be explained by dynamical relaxation in an initially circular disk. The previously claimed counterclockwise disk is not detected, despite the fact that we use higher-precision astrometric measurements and a larger FOV than in Lu et al. (2009) and Bartko et al. (2009). We confirm the kinematic structure seen by Bartko et al. (2009) at large radii, which may be a small cluster of stars that share similar motions but that are distinct from the CW disk seen at $r < 3\farcs2$.

Constraining the stars' line-of-sight distances through precise acceleration measurements is key for estimating stellar orbits and removes the need for prior assumptions that may lead to significant biases. Thus, it is critical to increase both the precision and the time baseline of astrometric measurements for stars at large radii from the SMBH. Furthermore, complete azimuthal coverage with spectroscopy at large radii will allow for the identification of more young stars and a better characterization of the dynamics of the off-disk population.

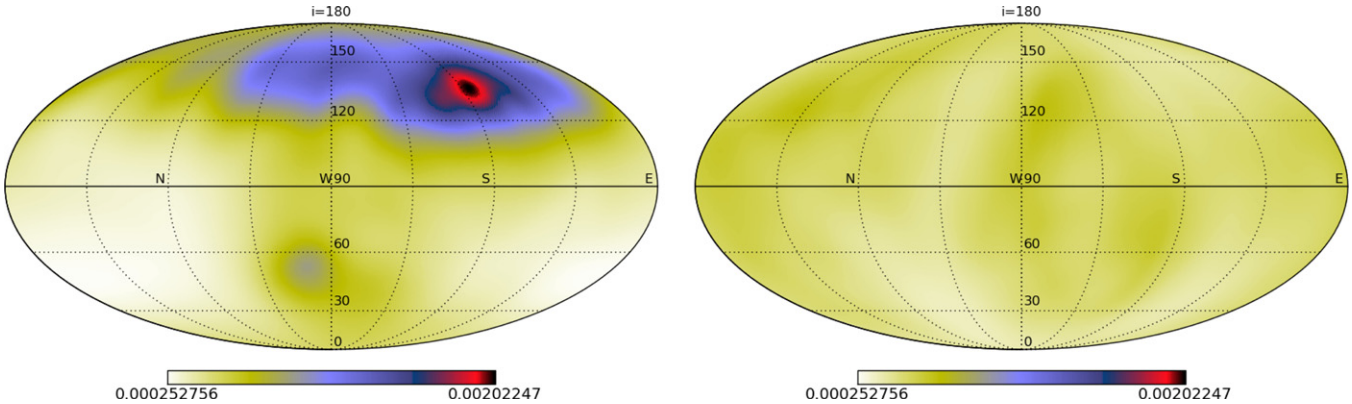

Figure 21. Left: density of normal vectors for the B stars (K $\geqslant$ 14) in our sample. The peak density, 0.002 stars deg^{-2}, is located at $(i, \Omega) = (136^\circ, 85^\circ)$. Right: density of normal vectors for an isotropically distributed sample of 18 stars. The same stretch is used for both density maps.

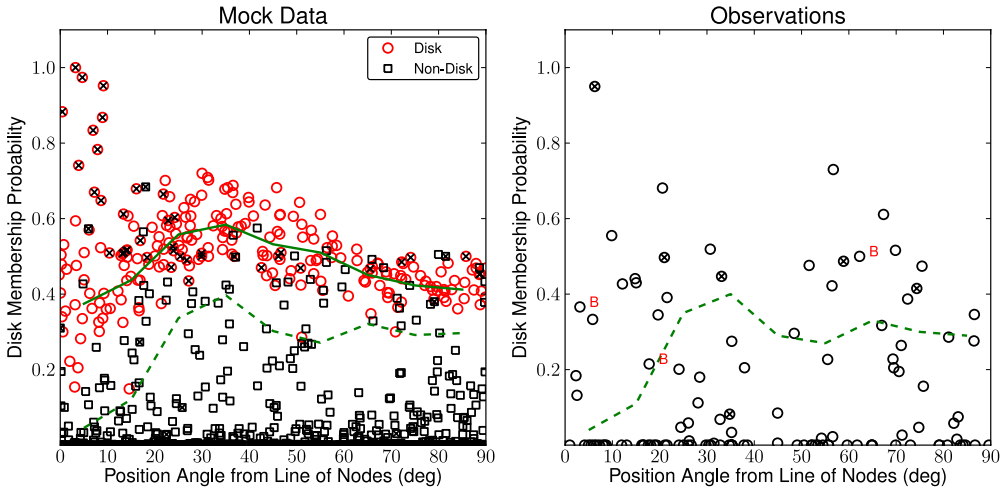

Figure 22. Left: disk membership probability plotted against position angle from the disk line of nodes ($\Omega = 96.^\circ3$) for the 10 simulations with $f_{\rm disk} = 0.2$. True disk members are shown as red circles ($N = 240$), while stars from the isotropic population are marked as black squares ($N = 960$). Stars with significant acceleration detections are marked with an "x." For disk stars, the probability of disk membership is a function of the angular offset from the disk's line of nodes. Non-accelerating disk stars with small angular offsets ($<20^\circ$) show relatively large scatter in disk membership probability. We compute the median and standard deviation of the probability in angular offset bins of 10° for all non-accelerating disk stars. The median and 3σ lower-limit values are shown as the green solid and dashed curves, respectively. Right: same plot, but for the observed sample of $N = 116$ stars. The 3σ lower-limit curve is overplotted. Points above this curve represent the most likely members of the clockwise disk. The 3 B stars that are likely disk members are indicated with the letter "B."

Support for this work was provided by the NSF grant AST-0909218. The authors thank the referee for useful comments that helped improve the paper. We are also grateful to Eric Becklin for the many helpful discussions about the project and to Brad Hansen for suggestions on the disk simulations. We thank Richard Alexander for generously providing updated eccentricity values from dynamical evolution models of the GC young stars. We thank the staff of the Keck Observatory for their help in obtaining the observations. S.Y. thanks the Aspen Center for Physics and the organizers of the summer 2012 workshop, as well as Ann-Marie Madigan for insightful discussions. The W. M. Keck Observatory is operated as a scientific partnership among the California Institute of Technology, the University of California and the National Aeronautics and Space Administration. The Observatory was made possible by the generous financial support of the W. M. Keck Foundation. The authors also recognize and acknowledge the very significant cultural role and reverence that the summit of Mauna Kea has always had within the indigenous Hawaiian community. We are most fortunate to have the opportunity to conduct observations from this mountain.

Facilities: Keck:II (NIRC2, OSIRIS), Keck:I (NIRC)

APPENDIX A

IMPROVED SPECKLE CAMERA (NIRC) DISTORTION SOLUTION

The AO images that have new corrections for geometric optical distortion and differential atmospheric refraction (DAR; Yelda et al. 2010) allow for an improvement in the determination of the geometric optical distortion for the speckle camera (NIRC; Matthews et al. 1996). We use a similar approach to that described in Lu et al. (2009), but here we map the speckle data to the predicted star list for the 2004 July speckle epoch (Appendix C) as opposed to the measured star positions. We note that DAR was inadvertently not corrected in the speckle images. However, over the 5″ speckle FOV, DAR amounts to ∼2 mas, in the extreme, and ∼1 mas, on average, and is somewhat reduced when the frames are averaged together because the field rotates on the detector throughout the speckle observations (in contrast to the AO observations, which are taken at a fixed P.A.). This new solution, given in Table 7, results in smaller

Table 7
Updated NIRC Reimager Distortion Coefficients

i	$X(a_i)$	$Y(b_i)$
0	1.2972×10^{-2}	-2.1134×10^{-2}
1	9.9726×10^{-1}	-1.1145×10^{-3}
2	-2.2849×10^{-3}	1.0034

residuals compared to our earlier solution (2 mas versus 3 mas, on average).

APPENDIX B

RESIDUAL RELATIVE ASTROMETRIC ERROR

The inaccuracies in the estimates of the PSF wings lead to an additional source of error that is not accounted for in the estimate of the centroiding error. Following the approach introduced by our group in Clarkson et al. (2012), we include an "additive" noise term for each observational approach. For the AO data, images taken in a consistent setup ($N = 11$ observations at the time of this analysis) to the 2006 June image were aligned. Once in a common reference frame, lines were fit to the positions as a function of time, where the positional uncertainties included the error on the mean from the three subset images for each epoch ($\sigma_{\rm rms}$; see Section 3.1) and the alignment errors ($\sigma_{\rm aln}$), which were determined by a half-sample bootstrap (Ghez et al. 2008). Confusion was accounted for, as described in Section 3.1.3. Only stars detected in all 11 epochs were used in this analysis. The velocity χ^2 distribution for 1024 stars was then compared to the expected distribution for 9 degrees of freedom (11 measurements − 2 fit parameters). We determined the amount of error to be added to the positional uncertainties in order to minimize, in a least squares sense, the difference between the distributions. This additive noise term for the AO data is $\sigma_{\rm add} = 0.1$ mas, comparable to the centroiding error of bright stars ($K < 15$).

The additive error for the speckle data was determined in a similar fashion, but we aligned all speckle and LGSAO data together and used the 2006 June image as the reference epoch. A line was to the speckle positions as a function of time, where again, the positional uncertainties included $\sigma_{\rm rms}$ and $\sigma_{\rm aln}$. Only stars that were detected in all 27 speckle images and that were not confused in any epoch were included in this analysis. In comparing the resulting χ^2 distribution for 32 stars to that expected for 25 degrees of freedom (27 speckle measurements − 2 fit parameters), a relatively small error (compared to $\sigma_{\rm rms}$ for speckle measurements, ∼1 mas for $K < 15$) of 0.18 mas is necessary to fully account for the positional scatter over time.

APPENDIX C

LOCAL DISTORTION CORRECTION

Of the 19 GC AO data sets taken at Keck since 2004, all but three have had identical observational setups (e.g., P.A. = 0 in the K' band). We began observing with a consistent setup (P.A. = 0° and same telescope pointings) in 2006 May and therefore refer to this as the "2006-setup." The 2004 July image was taken at P.A. = 200, while the 2005 July image was observed at P.A. = 190. In 2005 June, we observed the GC at P.A. = 0 but at a different starting position than the 2006-setup (see Ghez et al. 2008; Lu et al. 2009). In Yelda et al. (2010), we found that a data set observed at a non-zero P.A. can be transformed to the P.A. = 0 (2006-setup) image to ∼0.1 pix. To minimize the impact of this residual distortion when aligning the full GC data set, we applied a local distortion correction to the three images taken in different setups.

The local distortion correction was found by comparing the positions of the stars from the non-2006 epochs to their positions as predicted by their best-fit proper motions. This was done through the following series of steps. First, the 2006-setup star lists (taken through 2010) were transformed to the 2006 June epoch using a second-order polynomial. This epoch was chosen as the reference epoch as it is one of our highest quality images and is also the reference frame used in our main analysis (Section 3.1). The additive error term of 0.1 mas for AO data derived in Appendix B was included in the error measurements in these lists. Once the positions were placed in a common reference frame, proper motions were estimated by fitting a line to the positions as a function of time. Stars with proper motion errors >1.5 mas yr^{-1} or proper motions >10 mas yr^{-1} were excluded from this analysis, as they may be mismatched sources. Based on these proper motions, we created "predicted" star lists for each of the three non-2006-setup epochs.

We next transformed all of the AO data (through 2010), including the three epochs that were taken with a different setup, to the 2006 June image. The transformed stellar positions for the three non-2006-setups were then compared to their predicted positions based on the previous step. The differences in these positions represents the residual distortion in the images. The positional differences measured over the detector for each non-2006 epoch were smoothed into a local distortion map in the following way. For each pixel on the detector, the median positional difference of the five nearest stars was taken as the correction for that pixel. We note that the two data sets taken at a non-zero P.A. did not overlap completely with the 2006 June field, and we assigned the pixels with no overlap a value of zero. Similarly, we made a local distortion error map by taking

Table 8
Galactic Center Secondary IR Astrometric Standards

Name	K' (mag)	$T_{0,\rm IR}$ (year)	Radius (arcsec)	Δ R.A. (arcsec)	$\sigma_{\rm R.A.}$[a] (mas)	Δ Decl. (arcsec)	$\sigma_{\rm Decl.}$[a] (mas)	$v_{\rm R.A.}$[b] (mas yr^{-1})	$v_{\rm Decl.}$[b] (mas yr^{-1})
S0-3	14.8	2008.39	0.36	0.3351	1.1	0.1195	1.4	9.4 ± 0.4	-1.2 ± 0.6
S0-6	14.2	2008.30	0.36	0.0292	1.1	−0.3624	1.2	-5.2 ± 0.3	3.7 ± 0.4
S0-5	15.3	2007.99	0.41	0.1790	1.1	−0.3664	1.3	-2.1 ± 0.3	0.4 ± 0.5

Notes.
[a] Positional errors include centroiding, alignment, and residual distortion (1 mas) errors, but do not include error in position of Sgr A*.
[b] Velocity errors do not include error in velocity of Sgr A* (0.09 mas yr^{-1}, 0.14 mas yr^{-1} in R.A. and Decl., respectively).

(This table is available in its entirety in a machine-readable form in the online journal. A portion is shown here for guidance regarding its form and content.)

Table 9
Disk Membership Sample

Name	P.A.$_{nodes}$[a] (deg)	Sample[b]
S8-15	72.4	1σ
S4-169	9.9	1σ
S3-5	15.0	1σ
S7-10	75.5	1σ
irs34W	14.8	1σ
S7-161	5.8	1σ
S6-63	67.3	1σ
S3-10	12.1	1σ
S7-236	20.6	1σ
S2-21	51.6	1σ
S2-16	56.7	1σ
S1-8	62.3	1σ
S4-36	19.7	1σ
S1-3	74.4	1σ
S0-15	6.2	1σ
S1-12	58.9	1σ
S1-14	21.0	1σ
S10-32	3.1	1σ
S8-7	69.9	1σ
S6-82	2.3	2σ
irs34NW	30.7	2σ
irs9W	56.4	2σ
S2-19	86.5	2σ
irs16CC	21.6	3σ
S2-17	48.4	3σ
S3-190	17.8	3σ
irs16C	33.1	3σ
S1-21	2.5	3σ
S10-34	26.1	Other
S10-48	80.9	Other
S5-237	16.6	Other
S5-236	19.3	Other
S5-235	64.9	Other
S5-231	7.3	Other
S10-4	84.1	Other
S10-5	74.8	Other
S6-100	82.8	Other
S10-50	11.9	Other
S4-364	69.9	Other
S13-3	32.8	Other
S10-7	30.8	Other
S11-5	89.6	Other
S11-21	83.1	Other
S10-136	37.8	Other
S0-14	26.2	Other
S6-90	44.9	Other
S9-23	75.8	Other
S9-20	55.5	Other
S9-143	28.1	Other
S9-13	64.8	Other
S9-114	52.9	Other
S9-1	8.0	Other
S8-4	83.6	Other
S8-196	26.0	Other
S8-181	31.5	Other
S7-36	28.5	Other
S7-30	16.2	Other
S7-228	6.1	Other
S7-216	4.1	Other
S7-20	55.7	Other
S7-19	53.5	Other
S7-180	18.8	Other
S6-96	24.1	Other
S6-95	61.7	Other
S6-93	54.5	Other
S6-81	8.7	Other
S7-16	71.1	Other
irs16NW	86.7	Other
irs3E	52.2	Other
S3-3	5.5	Other
S3-26	44.9	Other
S3-25	70.6	Other
S3-2	16.5	Other
S3-19	67.0	Other
S2-76	79.1	Other
S2-74	86.5	Other
S2-7	69.3	Other
S2-6	32.8	Other
S3-30	54.2	Other
S2-58	21.6	Other
S2-4	37.9	Other
S2-22	1.0	Other
S1-33	6.6	Other
S1-24	59.7	Other
S1-22	24.1	Other
S1-2	81.1	Other
S1-19	69.5	Other
S1-18	56.6	Other
S1-1	8.3	Other
S2-50	35.2	Other
S3-314	5.0	Other
S3-331	65.0	Other
S3-374	52.1	Other
irs33N	84.7	Other
irs33E	71.2	Other
irs29N	35.2	Other
irs1W	13.0	Other
irs16SW-E	24.5	Other
irs16SW	34.8	Other
S9-283	21.1	Other
irs16NE	25.1	Other
irs13E4	29.8	Other
irs13E2	34.7	Other
irs13E1	35.3	Other
S6-89	35.3	Other
S5-34	38.6	Other
S5-191	50.5	Other
S5-187	79.1	Other
S5-183	30.4	Other
S4-71	73.0	Other
S4-287	82.2	Other
S4-262	18.1	Other
S4-258	26.7	Other
S3-96	17.6	Other
irs7SE	55.7	Other
S9-9	49.1	Other

Notes.
[a] Position angle offset from the line of nodes of the clockwise disk ($\Omega = 96.^{\circ}3$) with a range of 0°–90°.
[b] The level above which the star's disk membership probability falls for its respective angular offset bin (see Figure 22).

the standard deviation of the positional differences for the five nearest neighbors to each pixel.

We verified that this method reduced the residuals in the transformation of the P.A. = 200 to P.A. = 0 images from 2004 July. We applied this local distortion correction to the positions

in the star lists created by *StarFinder* (Diolaiti et al. 2000), and added the local distortion error in quadrature to the centroiding errors for the three non-2006 epochs.

APPENDIX D

UPDATED SGR A*-RADIO REST FRAME

Updated astrometry for the secondary standards originally presented in Yelda et al. (2010) is shown in Table 8. The updates reflect a new mosaicking procedure, which is done on the individual star lists as opposed to the images (see Section 3.1). As compared to the previous measurements reported in Yelda et al. (2010), we find several stars with $>3\sigma$ difference in either the X ($N = 6$ stars) or Y ($N = 19$ stars) velocity coordinate. However, the χ^2 value of the velocity fits improved in almost all cases with our new analysis, and we therefore use these updated values when constructing our reference frame. We present 1210 astrometric standards here, slightly fewer than Yelda et al. (2010), which had 1279 stars. This discrepancy is a result of the higher S/N in the overlapping regions of mosaicked images as compared to mosaicked star lists.

APPENDIX E

LINE OF NODES BIAS

Disk stars located near the disk's line of nodes ($\Omega = 96.^\circ3$) have a small line-of-sight distance ($|z| \sim 0$). For such stars, the acceleration prior may lead to biased orbital solutions. Unless the star has a detectable acceleration or an upper limit constraining the line-of-sight distance to $|z| > 0$, the line-of-sight distance is determined by randomly sampling from a uniform distribution of accelerations, bounded by the minimum and maximum allowed accelerations. With such a prior, a wide range of z's is allowed, most of which will be non-zero, thus leading to orbital solutions biased away from the nominal disk solution. The disk membership probability described in Section 4.1 will therefore be a function of the disk stars' locations along their orbit. To see this, we plot the disk membership probability against the P.A. relative to the disk line of nodes ($\Omega = 96.^\circ3$) for all stars in the 10 mock data sets with $f_{\rm disk} = 0.2$ (Figure 22, left panel). Note that the accelerating disk stars have high disk membership probability for small angles (these stars are the innermost stars in radius). We therefore compute the median and standard deviation of the probability in angular offset bins of 10° for all non-accelerating disk stars and use this as a metric for identifying the most likely members of the disk.

The observed data are shown in the right panel of Figure 22. We find that 28 stars have disk membership probabilities above the 3σ lower-limits for their respective P.A. bin. These stars are therefore the most likely members of the CW disk. Assuming a true disk fraction of 20%, we estimate that 3–4 of these stars may not be true disk members. The P.A. and the significance level above which the star falls (either 1σ, 2σ, or 3σ) are shown in Table 9.

REFERENCES

Alexander, R. D., Armitage, P. J., Cuadra, J., & Begelman, M. C. 2008, ApJ, 674, 927
Alexander, R. D., Begelman, M. C., & Armitage, P. J. 2007, ApJ, 654, 907
Alexander, T. 2007, arXiv:0708.0688
Allen, D. A., Hyland, A. R., & Hillier, D. J. 1990, MNRAS, 244, 706
Anderson, J., & van der Marel, R. P. 2010, ApJ, 710, 1032
Bartko, H., Martins, F., Fritz, T. K., et al. 2009, ApJ, 697, 1741
Bartko, H., Martins, F., Trippe, S., et al. 2010, ApJ, 708, 834
Bastian, N., Covey, K. R., & Meyer, M. R. 2010, ARA&A, 48, 339
Beloborodov, A. M., Levin, Y., Eisenhauer, F., et al. 2006, ApJ, 648, 405
Berukoff, S. J., & Hansen, B. M. S. 2006, ApJ, 650, 901
Blum, R. D., Depoy, D. L., & Sellgren, K. 1995, ApJ, 441, 603
Bonnell, I. A., & Rice, W. K. M. 2008, Sci, 321, 1060
Buchholz, R. M., Schödel, R., & Eckart, A. 2009, A&A, 499, 483
Christopher, M. H., Scoville, N. Z., Stolovy, S. R., & Yun, M. S. 2005, ApJ, 622, 346
Clarkson, W., Ghez, A., Morris, M., et al. 2012, ApJ, 751, 132
Cuadra, J., Armitage, P. J., & Alexander, R. D. 2008, MNRAS, 388, L64
Diolaiti, E., Bendinelli, O., Bonaccini, D., et al. 2000, A&AS, 147, 335
Do, T., Ghez, A. M., Morris, M. R., et al. 2009, ApJ, 703, 1323
Do, T., Lu, J. R., Ghez, A. M., et al. 2013, ApJ, 764, 154
Eckart, A., & Genzel, R. 1997, MNRAS, 284, 576
Eisenhauer, F., Genzel, R., Alexander, T., et al. 2005, ApJ, 628, 246
Fritz, T., Gillessen, S., Trippe, S., et al. 2010, MNRAS, 401, 1177
Genzel, R., Schödel, R., Ott, T., et al. 2003, ApJ, 594, 812
Gerhard, O. 2001, ApJL, 546, L39
Ghez, A. M., Becklin, E., Duchjne, G., et al. 2003, ANS, 324, 527
Ghez, A. M., Hornstein, S. D., Lu, J. R., et al. 2005a, ApJ, 635, 1087
Ghez, A. M., Klein, B. L., Morris, M., & Becklin, E. E. 1998, ApJ, 509, 678
Ghez, A. M., Morris, M., Becklin, E. E., Tanner, A., & Kremenek, T. 2000, Natur, 407, 349
Ghez, A. M., Salim, S., Hornstein, S. D., et al. 2005b, ApJ, 620, 744
Ghez, A. M., Salim, S., Weinberg, N. N., et al. 2008, ApJ, 689, 1044
Gillessen, S., Eisenhauer, F., Trippe, S., et al. 2009, ApJ, 692, 1075
Goodman, J. 2003, MNRAS, 339, 937
Górski, K. M., Hivon, E., Banday, A. J., et al. 2005, ApJ, 622, 759
Gürkan, M. A., & Rasio, F. A. 2005, ApJ, 628, 236
Haas, J., Šubr, L., & Kroupa, P. 2011a, MNRAS, 412, 1905
Haas, J., Šubr, L., & Vokrouhlický, D. 2011b, MNRAS, 416, 1023
Hansen, B. M. S., & Milosavljević, M. 2003, ApJL, 593, L77
Hobbs, A., & Nayakshin, S. 2009, MNRAS, 394, 191
Hopman, C., & Alexander, T. 2006, ApJ, 645, 1152
Hornstein, S. D. 2007, PhD thesis, Univ. of California, Los Angeles
Kim, S. S., Figer, D. F., & Morris, M. 2004, ApJL, 607, L123
Kocsis, B., & Tremaine, S. 2011, MNRAS, 412, 187
Kolykhalov, P. I., & Syunyaev, R. A. 1980, SvAL, 6, 357
Krabbe, A., Genzel, R., Drapatz, S., & Rotaciuc, V. 1991, ApJL, 382, L19
Krabbe, A., Genzel, R., Eckart, A., et al. 1995, ApJL, 447, L95
Larkin, J., Barczys, M., Krabbe, A., et al. 2006, NewAR, 50, 362
Levin, Y. 2007, MNRAS, 374, 515
Levin, Y., & Beloborodov, A. M. 2003, ApJL, 590, L33
Levin, Y., Wu, A., & Thommes, E. 2005, ApJ, 635, 341
Lin, D. N. C., & Pringle, J. E. 1987, MNRAS, 225, 607
Löckmann, U., & Baumgardt, H. 2009, MNRAS, 394, 1841
Löckmann, U., Baumgardt, H., & Kroupa, P. 2009, MNRAS, 398, 429
Lu, J. R., Do, T., Ghez, A. M., et al. 2013, ApJ, 764, 155
Lu, J. R., Ghez, A. M., Hornstein, S. D., Morris, M., & Becklin, E. E. 2005, ApJL, 625, L51
Lu, J. R., Ghez, A. M., Hornstein, S. D., et al. 2009, ApJ, 690, 1463
Lucas, W. E., Bonnell, I. A., Davies, M. B., & Rice, W. K. M. 2013, MNRAS, 433, 353
Madigan, A., Levin, Y., & Hopman, C. 2009, ApJL, 697, L44
Madigan, A.-M., Levin, Y., Pfuhl, O., Genzel, R., & Perets, H. B. 2013, arXiv:1305.1625
Mapelli, M., Hayfield, T., Mayer, L., & Wadsley, J. 2008, arXiv:0805.0185
Mapelli, M., Hayfield, T., Mayer, L., & Wadsley, J. 2012, ApJ, 749, 168
Matthews, K., Ghez, A. M., Weinberger, A. J., & Neugebauer, G. 1996, PASP, 108, 615
Matthews, K., & Soifer, B. T. 1994, ExA, 3, 77
Meyer, L., Ghez, A. M., Schödel, R., et al. 2012, Sci, 338, 84
Morris, M. 1993, ApJ, 408, 496
Najarro, F., Krabbe, A., Genzel, R., et al. 1997, A&A, 325, 700
Nayakshin, S. 2006, MNRAS, 372, 143
Nayakshin, S., & Cuadra, J. 2005, A&A, 437, 437
Nayakshin, S., Cuadra, J., & Springel, V. 2007, MNRAS, 379, 21
Paumard, T., Genzel, R., Martins, F., et al. 2006, ApJ, 643, 1011
Rafelski, M., Ghez, A. M., Hornstein, S. D., Lu, J. R., & Morris, M. 2007, ApJ, 659, 1241
Rauch, K. P., & Tremaine, S. 1996, NewA, 1, 149
Reid, M. J., Menten, K. M., Trippe, S., Ott, T., & Genzel, R. 2007, ApJ, 659, 378
Sanders, R. H. 1992, Natur, 359, 131

Schödel, R., Merritt, D., & Eckart, A. 2009, A&A, 502, 91
Schödel, R., Ott, T., Genzel, R., et al. 2003, ApJ, 596, 1015
Schödel, R., Yelda, S., Ghez, A., et al. 2013, MNRAS, 429, 1367
Shlosman, I., & Begelman, M. C. 1987, Natur, 329, 810
Šubr, L., Schovancová, J., & Kroupa, P. 2009, A&A, 496, 695
Tamblyn, P., Rieke, G. H., Hanson, M. M., et al. 1996, ApJ, 456, 206
Trippe, S., Gillessen, S., Gerhard, O. E., et al. 2008, A&A, 492, 419
Wardle, M., & Yusef-Zadeh, F. 2008, ApJL, 683, L37
Yelda, S. 2012, PhD thesis, Univ. of California, Los Angeles
Yelda, S., Lu, J. R., Ghez, A. M., et al. 2010, ApJ, 725, 331
Yu, Q., Lu, Y., & Lin, D. N. C. 2007, ApJ, 666, 919
Yusef-Zadeh, F., & Wardle, M. 2008, in ASP Conf. Ser. 387, Massive Star Formation: Observations Confront Theory, ed. H. Beuther, H. Linz, & T. Henning (San Francisco, CA: ASP), 361